This manuscript is an EarthArXiv preprint and has been submitted for publication in GEOLOGY. Please note that this manuscript has not been peer-reviewed. Subsequent versions of this manuscript may therefore have slightly different content. If accepted, the final version of this manuscript will be available via the “Peer-reviewed Publication DOI” link on the right-hand side of this webpage. Please feel free to contact any of the authors directly. We welcome your feedback.

Autogenic initiation of basin-scale salt tectonics

Jimmy Moneron[1,2], Giridas Maiti[1], Mads Huuse[3], Christopher Aiden-Lee Jackson[4,5], Alexandre Lethiers[2], and Nevena Andrić-Tomašević[1]

[1]*Institute of Applied Geosciences, Karlsruhe Institute of Technology, Germany*

[2]*ISTeP, Sorbonne Université, CNRS, 75005, Paris, France*

[3]*Department of Earth and Environment, The University of Manchester, Manchester, UK*

[4]*WSP UK Ltd, 8 First Street, Manchester, M15 4RP, UK*

[5]*Landscape and Basins Research Group (LBRG), Department of Earth Science and Engineering, Imperial College London, London SW7 2AZ, UK*

ABSTRACT

Salt structures typically form due to the post-depositional flow of salt triggered and maintained by allogenic drivers such as differential loading, gravity gliding, or shortening. Using ~26,000 km² of 3-D seismic reflection data and 34 wells from the Southern North Sea, we propose that the earliest regional deformation of the Southern Permian Basin salt giant (Zechstein Supergroup) was instead autogenic, being initiated by intra-salt diagenetic processes. The synclines of the earliest salt-cored folds overlie ridges of intrasalt gypsum that converted to anhydrite at the end of the Permian. Triassic onlap and truncation show that these folds formed immediately after salt deposition, long before regional Paleogene–Neogene shortening, and that the curvilinear, variably oriented hinges parallel neither the sub-salt fault network nor the dip of the detachment, as allogenic mechanisms would predict. Numerical experiments show that the density contrast created by intrasalt diagenesis may have caused the gypsum ridges to founder into the underlying halite, drawing down the depositional surface, forming depressions ultimately filled by Triassic sediment. A significant component of early-stage salt tectonics in the Southern Permian Basin may therefore be autogenic in origin, with the distribution of the much younger shortening structures being

dictated by diagenetic reactions within the evaporite rather than by regional, plate-driven stresses. Regional tectonism subsequently amplified these structures, which nonetheless retain a record of key control on their distribution.

INTRODUCTION

Salt tectonics is conventionally attributed to allogenic controls with gravity as the driver, acting on an overburden of uneven thickness or on a tilted base; and tectonic events supplying the trigger, whether through sub-salt basement reactivation or far-field shortening (Jackson and Hudec, 2017). In layered evaporite sequences (LESs; Rowan et al., 2019), the internal stratigraphy of the salt, notably its competent carbonate and sulfate layers, is typically treated as a passive strain marker and may provide insights into the trigger, style, and driver of salt flow.

Imaged almost continuously by three-dimensional (3-D) seismic data, extensively drilled (Fig. S1), and only moderately deformed, the Southern Permian Basin (SPB) is an exceptional laboratory in which to test that assumption. This E–trending intracratonic basin (Ziegler, 1990) contains the Zechstein Supergroup (ZSG) (Lopingian), which was deposited in five evaporite cycles (Z1–Z5; Smith and Crosby, 1979; Taylor, 1998; Fig. 1). The most prominent stratigraphic internal marker, the Z3 anhydrite (Z3a), produces high-amplitude reflections mappable basin-wide (the “Z3a stringer”; Mattes and Conway Morris, 1990; van Gent et al., 2011).

The ZSG was repeatedly remobilized into stocks, walls, and salt-cored folds (Brennan et al., 2023). Halokinesis began in the Triassic in response to sub-salt fault reactivation and sediment loading, continued during Jurassic–Early Cretaceous rifting, and culminated in Late Cretaceous–Paleogene shortening that squeezed pre-existing diapirs and generated salt-detached buckle folds (Stewart and Coward, 1995; Geluk, 1999; Brennan and Adam, 2023).

Each of these allogenic mechanisms predicts structures parallel to sub-salt faults or depocenter axes, or perpendicular to the regional shortening direction.

Across the SPB, Z3a contains a network of anomalously thick zones (ATZs); these are curvilinear ridges of former gypsum, now anhydrite, that occupy about one third of the unit volume and show no preferred orientation or relation to basement structure (van Gent et al., 2011; Moneron, 2025). Their conversion to anhydrite during deposition of the overlying Z3 salts made them ~700 kg/m³ denser than the underlying halite (Moneron and Jackson, 2025), and their sinking folded the stringer into synclines cored by the ATZs (Aldridge et al., 2026). Should foundering of the ATZs also draw the overlying halite downwards, generating a depression at the depositional surface? Whether intrasalt folding is the only record of this process remains untested.

Stratigraphic framework of Zechestin and Meso-Cenoizoic units (Fig. S2), the ATZ network, and earlier models of regional salt tectonics are reviewed in the Supplemental Material.

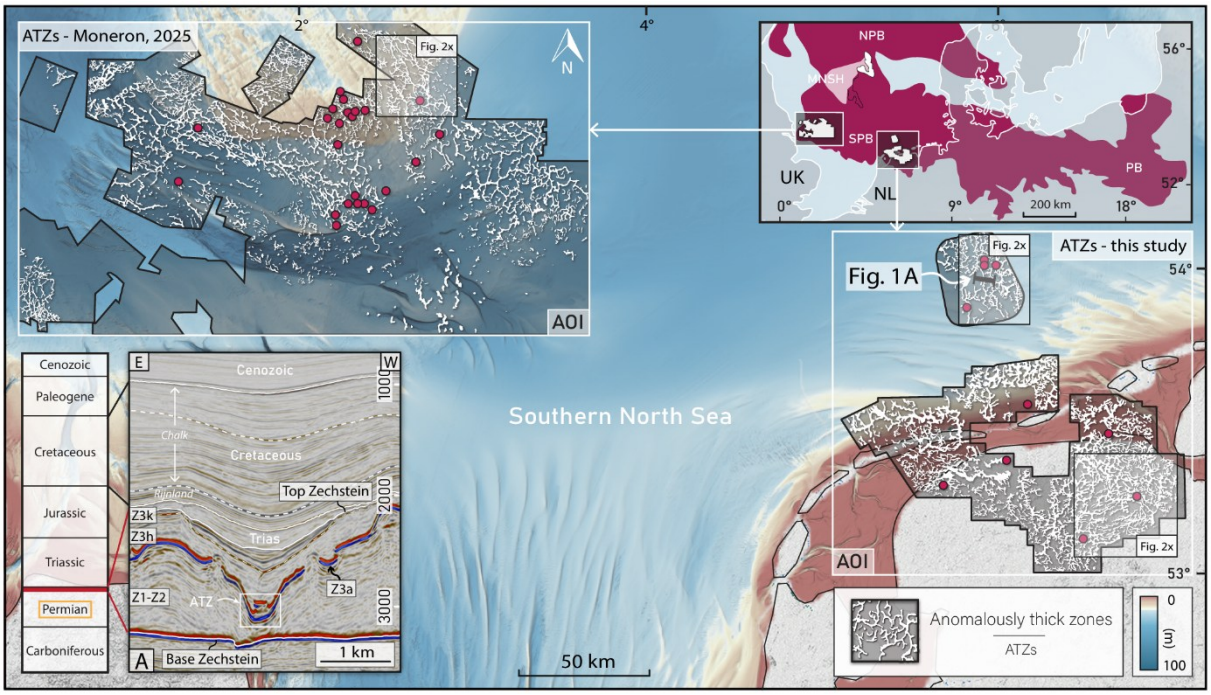


Figure 1. Setting and Z3 anhydrite (Z3a) network of anomalously thick zones (ATZs). Inset: Southern Permian Basin (SPB), adjacent basins (NPB, Northern Permian Basin; PB, Polish Basin; MNSH, Mid North Sea High) and Zechstein extent. Main panels: ATZ network (white) in the UK and Dutch areas of interest (AOIs), with 3-D seismic coverage (outlines) and wells (circles). (A) Seismic section through the UK AOI: an ATZ cores a syncline that persists into the Cenozoic. Full chronostratigraphy in the Supplemental Material (Fig. S2).

DATA AND METHODS

Data

We interpreted ~26,000 km² of 3-D seismic reflection data from the UK and Dutch sectors of the Southern North Sea tied to 34 wells from the national repositories (Fig. S1). The data are zero-phase and displayed with SEG reverse and normal polarities (insets of Fig. 2D). At the Z3a level, a dominant frequency of 25–30 Hz and interval velocity of 5000–6000 m/s give a limit of separability ($\lambda/4$) of ~50 m (Supplemental Material).

Horizon interpretation

Six horizons were tied to wells and mapped regionally: Base ZSG, Base Z3a, Top Z3a, Top ZSG (= Base Triassic), Top Bunter (= Base Rijnland), and Base Cretaceous (= Base Chalk). ATZs were delineated from the Z3a isopach using a 55 m threshold (Fig. 2E), which marks both the upper limit of the background thickness population and the thickness above which the Z3a exceeds the limit of separability. The network was also traced from root-mean-square (RMS) amplitude map extracted from the Top Z3a horizon, or the Base Z3a where the Top is discontinuous.

Numerical modeling

We modeled the gravitational sinking of dense anhydrite ATZs within halite by solving the 2-D incompressible Stokes equations for a Newtonian viscous rheology, with finite differences on a staggered grid and Lagrangian markers (Gerya and Yuen, 2003, 2007). The reference

domain (5 × 1 km, 10 m resolution) and contains four ATZs, 200 m wide and 150 m thick, spaced 1 km apart and joined by a 50-m-thick basal anhydrite layer, matching the definition of ATZs (van Gent et al., 2011; Moneron et al., 2025) and fitting our dataset observations. Halite and anhydrite densities are 2200 and 2900 kg/m^3, and viscosities 10^{17} and 10^{19} Pa s (Koyi, 2001; Burchardt et al., 2011, 2012). The system first evolves under its own weight; the deformed configuration is then overlain by material with sand density (2400 kg/m^3) and viscosity (10^{19} Pa·s), to test its response to loading. Other model experiments include ATZs detached from the basal layer, as well as variations in ATZ-halite density and viscosity contrasts, and ATZ size and spacing (Supplemental Material).

RESULTS

The Z3a and its anomalously thick zones

In both sectors, the Z3a is a continuous, high-amplitude reflection doublet that is positive at its top (tZ3a) and negative at its base (bZ3a). Well data indicate it is dominated by anhydrite (Figs. 2D, S2).

In plan view, ATZs form a dense, interconnected network (Figs. 2A–2C), enclosing polygonal cells of background-thickness Z3a. The fact that the network is resolved independently by both amplitude and thickness, in two areas, mapped with different surveys, establishes it as a property of the Z3a rather than an artifact of either method.

The Z3a thickness distribution is bimodal (Fig. 2E): a narrow background population centered on ~47 m covers 67% of the mapped area, and a distinct, long-tailed ATZ population covers the remaining 33%, decaying from a mode at 55–58 m to >127 m. The break at 55 m, just above the limit of seismic separability, provides an objective criterion to separate ATZs from

the background Z3a, so that the network compared with the overburden in Figure 3 is defined independently of the structures it is compared with.

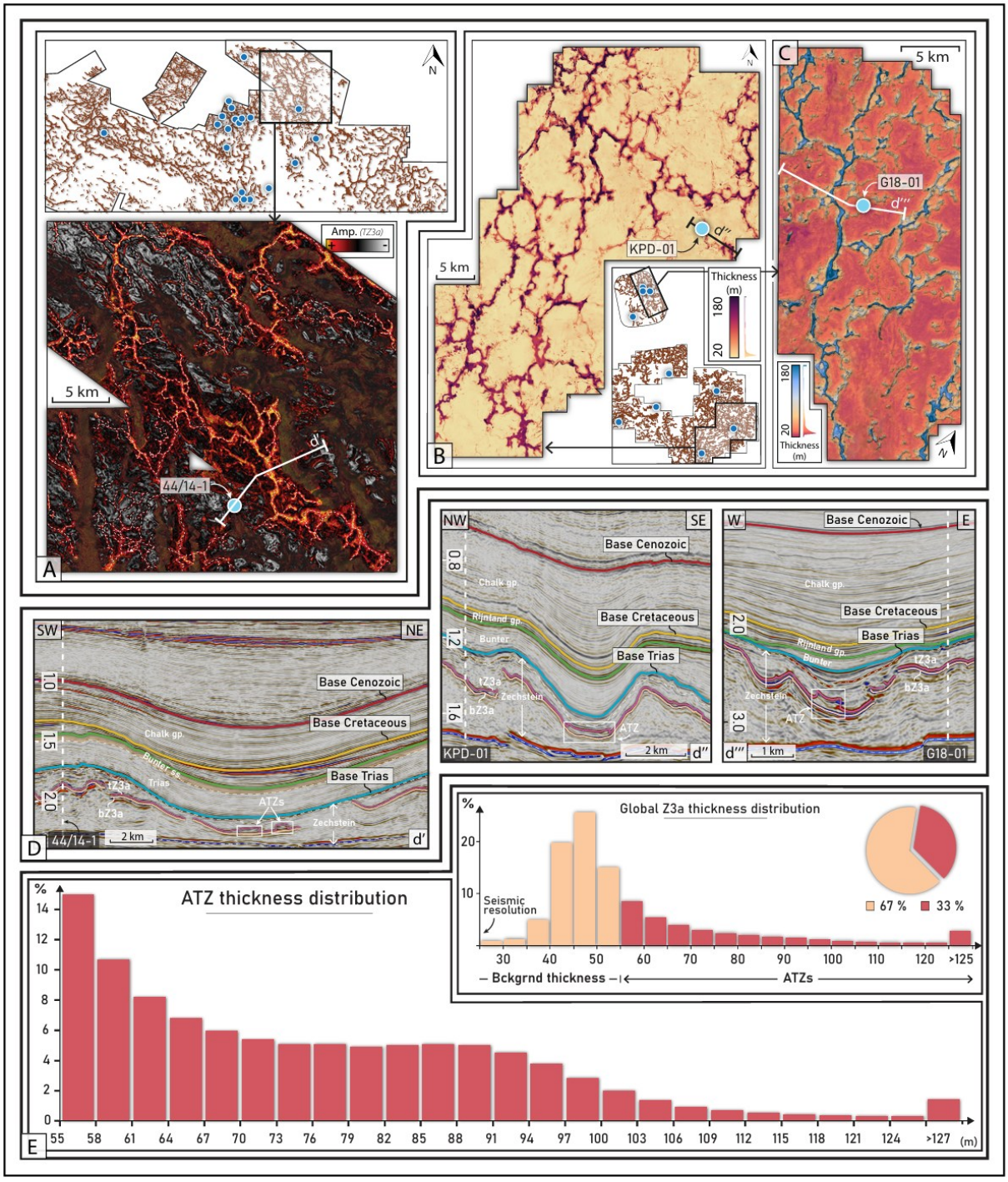


Figure 2. Distribution, thickness and seismic expression of the Z3a ATZ network. **(A)** UK sector: root-mean-square amplitude on the Top Z3a. **(B, C)** Dutch sector: Z3a isopachs. **(D)** Sections (d′, d″, d‴) tied to wells 44/14-1, KPD-01 and G18-01, showing ATZs in the cores of synclines expressed upward to the Base Cenozoic (enlarged in Fig. S3). **(E)** ATZ thickness distribution (inset: full Z3a). tZ3a, bZ3a: top and base Z3 anhydrite.

ATZs and regional synclines

ATZs underlie the synclines of a subset of the large salt-cored buckle folds that deform Mesozoic and Cenozoic strata (Fig. 3). They trend parallel to the hinges of the overlying synclines for tens of kilometers, including through sharp changes in trend; where the ridges bifurcate, so do the synclines, and isolated ATZ mounds underlie equant depressions. This relationship is observed in both sectors.

The relationship is not universal, however: some synclines of comparable wavelength and amplitude lack an underlying ATZ, and parts of the network lie where the ZSG is undeformed. Only where the two coincide, however, does the overburden record the geometries described below.

Syn-kinematic stratal geometries

Above ATZ-cored synclines, Lower Triassic reflections onlap the fold flanks, whereas Upper Triassic strata are more tabular and isopachous, extend beyond the synclines, and are folded across the adjacent anticlines (Figs. 3a′, 3a″, 3b′). Across the anticline crests, the Upper Triassic is locally truncated by the Base Cretaceous Unconformity (Figs. 3b″, 3c′).

Where synclines of comparable geometry lack an ATZ, none of these relationships are observed: instead, the entire Triassic sequence is isopachous across the fold hinge, and its reflections are parallel and conformable, without onlap (Fig. S7). These folds therefore post-Triassic.

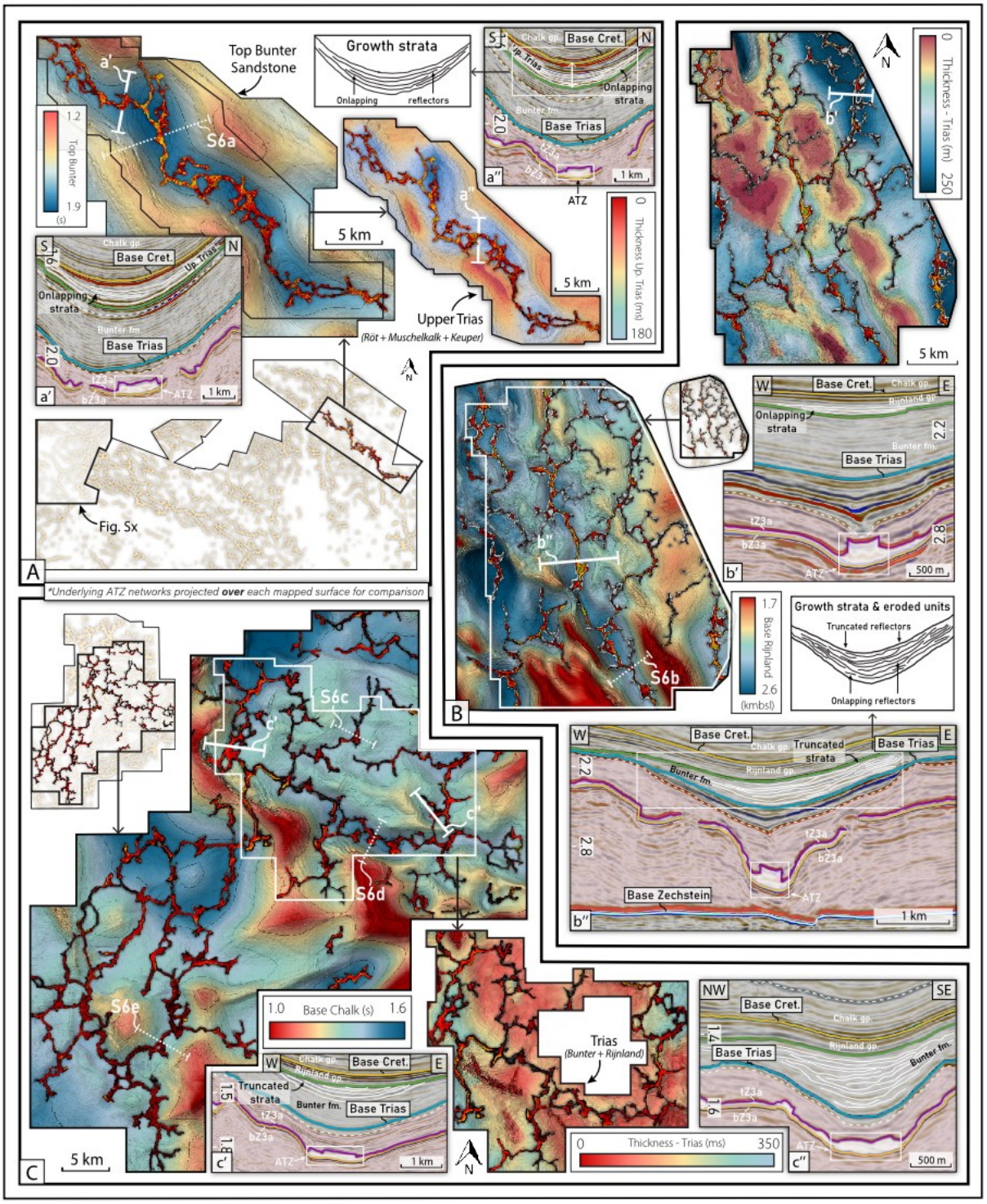


Figure 3. ATZs, post-salt synclines, and the stratal geometries above them. ATZ network (dark red) overlain on each map. **(A)** UK sector: Top Bunter time-structure and Upper Triassic isopach; a′ and a″ show Lower Triassic onlap onto the flanks of ATZ-cored synclines (inset defines the geometry). **(B)** Dutch sector: Base Rijnland depth-structure and Triassic isopach; b′ shows onlap, and b″ Triassic strata truncated beneath the Base Cretaceous over the flanking high. **(C)** Dutch sector: Base Chalk time-structure and Triassic isopach; c′ and c″ show the same relationships. Enlarged sections, maps without the overlay, and regional sections in Figs. S4–S6.

MODELING AND DISCUSSION

Model results

The models test whether ATZ sinking can generate the observed folds. Sinking begins after the conversion of gypsum to anhydrite (c.f. Moneron and Jackson, 2025), when densified ATZs is encased in halite (Fig. 4A, Stage 1).

The ATZs sink at 1–2 mm/yr while the interconnecting segments of the (Z3a) anhydrite layer rise at 1–1.5 mm/yr, producing ATZ-cored synclines separated by anticlines, with negligible lateral shortening (Fig. 4A, Stages 2–3). The deformation is transmitted upward through the overlying halite, depressing the upper surface directly above each sinking ATZ, forming depressions ~300 m deep and 400–500 m wide within 200 k.y.

Under a sand load (Fig. 4A, Stages 4–5), subsidence above the ATZs continues, deepening the synclines by a further ~50 m over 1 m.y. as halite is expelled toward the flanking anticlines. The inherited depressions thus evolve into minibasins resembling the observed Triassic lows observed in seismic data (Fig. 3).

Parametric studies reveal density and viscosity contrasts mainly govern sinking rates, whereas ATZ size and spacing determine the amplitude and wavelength of the folds (Figs. S13–S16). Detached ATZs sink faster (~4–5 mm/yr) and reach the base of the salt within 135 k.y., whereas attached ATZs, restrained by the layer, remain suspended (Figs. S9–S11); a more viscous layer further slows ATZ sinking.

INTERPRETATION AND DISCUSSION

Evolutionary Model

Every mechanism previously invoked for regional salt tectonics in the SPB is allogenic, predicting the formation of folds whose trend is determined externally (Stewart and Coward, 1995; Cloetingh et al., 1999; Deckers and van der Voet, 2018; Gaitan and Adam, 2023). We show that the ATZ-cored synclines track the curvilinear, almost random orientation of the ATZ network, and that only they preserve Triassic growth strata. Based on this, we argue that the formation and distribution of the earliest folds was instead autogenic, being controlled by the salt itself.

The causal sequence rests on a different line of evidence (Fig. 4B). We propose that gypsum ridges grew on the Zechstein depositional surface (T1; Moneron, 2025) and, once buried beneath Z3 halite, converted to anhydrite, which is stable at shallow burial in NaCl-saturated brine (Hardie, 1967). The conversion is dated in the SPB by collapse structures in and above the overlying halite (T2; Moneron and Jackson, 2025). The density inversion thus predates the Triassic extension and associated loading conventionally invoked to explain the initiation of basin-scale salt tectonics. The densified ATZs then foundered into underlying halite, folding the stringer (Aldridge et al., 2026) and drawing the top of the salt down into synclines wider than the ridges (T3). Foundering began in the Lopingian, but its surface expression is first recorded in the earliest Triassic by Lower Triassic onlap, whereas truncation of the Upper Triassic beneath the Base Cretaceous Unconformity over the intervening highs brackets minibasin growth (T4). Our models show that the density contrast alone suffices to produce this sequence of events (Fig. 4A).

In both the seismic data and the models, the depressions are much wider (2–5 km) than the ATZs (0.5–1 km) (Fig. 3), and 400–500 m above 200-m-wide blocks (Fig. 4A). Each ATZ is attached to the Z3a, which is more viscous than the encasing halite and cannot bend sharply; as the ATZ sinks it therefore drags the adjacent layer down, and the layer sags over a width

set by its thickness and viscosity, rather than by the size of the ATZ alone (Ribe, 2001). A ridge a few hundred meters across can thus produce a kilometer-scale depression.

Sediment then accumulates preferentially in the depressions, and the system enters the regime of density-driven minibasin subsidence familiar from other salt basins (Hudec et al., 2009; Fernandez et al., 2020): the sediment load expels salt from beneath the depocenter, amplifying the relief that created the accommodation and eventually welding the salt beneath the synclinal axes. Thereafter, subsidence no longer depends on the anhydrite-halite density contrast. Model sinking rates (1–2 mm/yr attached, ~4–5 mm/yr detached) are comparable to those modeled for anhydrite blocks in Newtonian salt (~2–13 mm/yr; Koyi, 2001; Burchardt et al., 2012), and sinking slows markedly once the underlying halite thins to 100–200 m.

Why connected anhydrite ridges never hit rock bottom

Intrasalt density inversion models predict that dense anhydrite founders to the base of the salt, a configuration rarely observed in natural systems (Koyi, 2001; Chemia et al., 2008; Strozyk et al., 2012). Our models reproduce this outcome only for ATZs detached from the Z3a, and the seismic data show the same contrast: the few detached ATZs rest on the base of the salt (Fig. S8), whereas attached ATZs, which form most of the network, lie several hundred meters above it (Fig. 2D). ATZs rarely reach the base of the salt because most remain attached, not because the density inversion is ineffective. The ATZ dynamic pressure anomaly is spread along the Z3A layer rather than confined to the ATZ only (Fig. S10), so the gradients that expel halite from beneath them are gentler; at such low stresses halite creep slows by orders of magnitude (Rowan et al., 2019), and attached ATZs remain suspended over geological time.

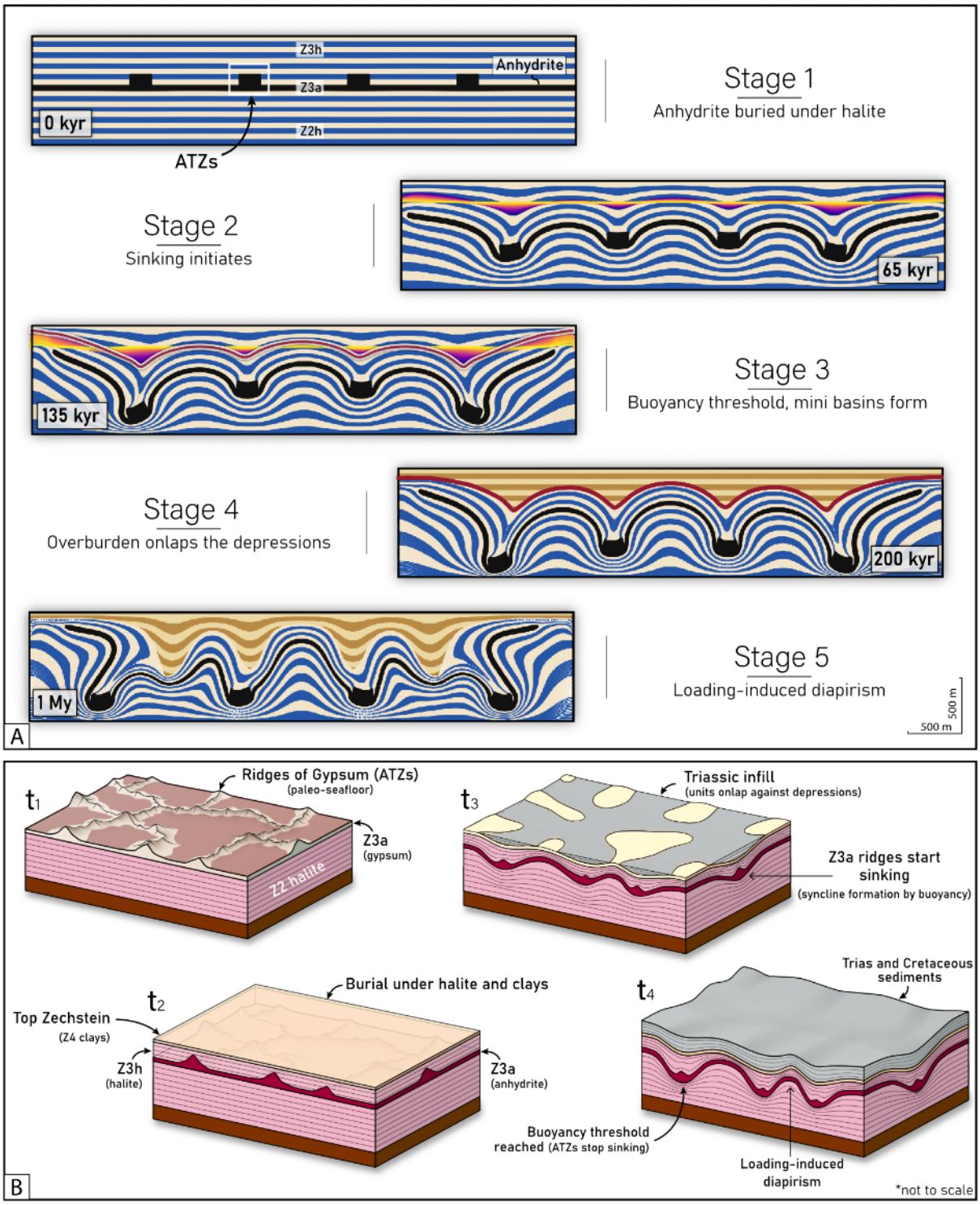


Figure 4. Numerical and conceptual models of ATZ foundering and minibasin nucleation. (A) Model evolution: Z3a layer (black) with four ATZs in halite (blue and cream markers), from densified ATZs (Stage 1) through foundering (Stages 2–3) to sediment loading (Stages 4–5); full evolution in Fig. S12 and parameters in Table S2. (B) Conceptual model (T1–T4) for the genesis of Triassic depressions above sinking ATZs.

Implications and limitations

The internal stratigraphy of a LES can define the structures that develop above it, rather than merely record salt flow (Strozyk et al., 2012; Raith et al., 2016; Moneron and Gvirtzman, 2025), with bearing on weld position and seal integrity for subsurface storage (Caglayan et al., 2020). The same latent instability should exist wherever sulfate was deposited as gypsum and later converted to anhydrite (Warren, 2006; Célini et al., 2024). Two-dimensional model limitations are provided in the Supplemental Material.

CONCLUSIONS

In the Southern North Sea, a distinct population of regional salt-cored folds is organized by anomalously thick zones of the Z3 anhydrite: only above these do Triassic strata thicken into the synclines and onlap their flanks, with truncation over the intervening highs. The density contrast created by gypsum-to-anhydrite conversion suffices to founder the ATZs, to deflect the depositional surface over a width exceeding their own, and to nucleate minibasins whose load then drove salt withdrawal and welding. Because the ATZs remain part of a continuous layer, their foundering is self-limiting.

The position of these structures was therefore set from within the evaporite, by a diagenetic reaction, before any of the allogenic mechanisms conventionally invoked was imposed. The internal stratigraphy of a salt giant initiated, rather than merely recorded, its deformation.

REFERENCES CITED

Aldridge, B., Stewart, S., Phillips, D., Foschi, M. and Cartwright, J. (2026). A new mode of syn-depositional folding in the Zechstein Supergroup due to differential loading and diagenetically induced density inversion. *Journal of Structural Geology*, 203, 105606. https://doi.org/10.1016/j.jsg.2025.105606

Brennan, C. and Adam, J. (2023). Regional variability of onset and cessation of salt tectonics in the Mesozoic and Cenozoic Southern North Sea subbasins. *AAPG Bulletin*, 107(12), 2169–2196.

Brennan, C., Preiss, A. and Adam, J. (2023). Three-dimensional seismic classification of salt structure morphologies across the Southern North Sea. *AAPG Bulletin*, 107(12), 2141–2167. https://doi.org/10.1306/08072221136

Burchardt, S., Koyi, H. and Schmeling, H. (2011). Strain pattern within and around denser blocks sinking within Newtonian salt structures. *Journal of Structural Geology*, 33, 145–153. https://doi.org/10.1016/j.jsg.2010.11.007

Burchardt, S., Koyi, H., Schmeling, H. and Fuchs, L. (2012). Sinking of anhydrite blocks within a Newtonian salt diapir: modelling the influence of block aspect ratio and salt stratification. *Geophysical Journal International*, 188, 763–778. https://doi.org/10.1111/j.1365-246X.2011.05290.x

Caglayan, D.G., Weber, N., Heinrichs, H.U., Linßen, J., Robinius, M., Kukla, P.A. and Stolten, D. (2020). Technical potential of salt caverns for hydrogen storage in Europe. *International Journal of Hydrogen Energy*, 45, 6793–6805.

Célini, N., Pichat, A. and Ringenbach, J.-C. (2024). Salt tectonics synchronous with salt deposition in the Santos Basin (Ariri Formation, Brazil). *Earth and Planetary Science Letters*, 641, 118853. https://doi.org/10.1016/j.epsl.2024.118853

Chemia, Z., Koyi, H. and Schmeling, H. (2008). Numerical modelling of rise and fall of a dense layer in salt diapirs. *Geophysical Journal International*, 172(2), 798–816. https://doi.org/10.1111/j.1365-246X.2007.03661.x

Cloetingh, S., Burov, E. and Poliakov, A. (1999). Lithosphere folding: primary response to compression? (from central Asia to Paris basin). *Tectonics*, 18(6), 1064–1083. https://doi.org/10.1029/1999TC900040

Deckers, J. and van der Voet, E. (2018). A review on the structural styles of deformation during Late Cretaceous and Paleocene tectonic phases in the southern North Sea area. *Journal of Geodynamics*, 115, 1–9.

Fernandez, N., Hudec, M.R., Jackson, C.A.-L., Dooley, T.P. and Duffy, O.B. (2020). The competition for salt and kinematic interactions between minibasins during density-driven subsidence: observations from numerical models. *Petroleum Geoscience*, 26(1), 3–15. https://doi.org/10.1144/petgeo2019-051

Gaitan, G. and Adam, J. (2023). Extent and variability of Mesozoic–Cenozoic multi-stage salt diapirs in the Southern Permian Basin, Southern North Sea. *Basin Research*, 35(6), 2078–2117. https://doi.org/10.1111/bre.12791

Geluk, M.C. (1999). Late Permian (Zechstein) rifting in the Netherlands: models and implications for petroleum geology. *Petroleum Geoscience*, 5(2), 189–199.

Gerya, T.V. and Yuen, D.A. (2003). Characteristics-based marker-in-cell method with conservative finite-differences schemes for modeling geological flows with strongly variable transport properties. *Physics of the Earth and Planetary Interiors*, 140, 293–318. https://doi.org/10.1016/j.pepi.2003.09.006

Gerya, T.V. and Yuen, D.A. (2007). Robust characteristics method for modelling multiphase visco-elasto-plastic thermo-mechanical problems. *Physics of the Earth and Planetary Interiors*, 163, 83–105. https://doi.org/10.1016/j.pepi.2007.04.015

Hardie, L.A. (1967). The gypsum–anhydrite equilibrium at one atmosphere pressure. *American Mineralogist*, 52, 171–200.

Hudec, M.R., Jackson, M.P.A. and Schultz-Ela, D.D. (2009). The paradox of minibasin subsidence into salt: clues to the evolution of crustal basins. *GSA Bulletin*, 121(1–2), 201–221.

Jackson, M.P.A. and Hudec, M.R. (2017). *Salt Tectonics: Principles and Practice*. Cambridge: Cambridge University Press.

Koyi, H.A. (2001). Modeling the influence of sinking anhydrite blocks on salt diapirs targeted for hazardous waste disposal. *Geology*, 29, 387–390. https://doi.org/10.1130/0091-7613(2001)029<0387:MTIOSA>2.0.CO;2

Mattes, B.W. and Conway Morris, S. (1990). Carbonate/evaporite deposition in the Late Precambrian–Early Cambrian Ara Formation of Southern Oman. *Geological Society, London, Special Publications*, 49(1), 617–636.

Moneron, J. (2025). Major heterogeneity in evaporitic depositional systems: the genesis of kilometre-scale gypsum networks in the Zechstein Basin. *Global and Planetary Change*, 246, 104710. https://doi.org/10.1016/j.gloplacha.2025.104710

Moneron, J. and Jackson, C.A.-L. (2025). Basin-scale development of giant collapse structures induced by gypsum diagenesis. *Geology*, 53(8), 673–678. https://doi.org/10.1130/G53338.1

Moneron, J., & Gvirtzman, Z. (2025). Multiphase deformation of a multilayered salt giant: Salt tectonics in the Levant Basin. *Geological Society of America Bulletin*, *137*(11-12), 4919-4937.

Raith, A.F., Strozyk, F., Visser, J. and Urai, J.L. (2016). Evolution of rheologically heterogeneous salt structures: a case study from the NE Netherlands. *Solid Earth*, 7(1), 67–82. https://doi.org/10.5194/se-7-67-2016

Ribe, N.M. (2001). Bending and stretching of thin viscous sheets. *Journal of Fluid Mechanics*, 433, 135–160.

Rowan, M.G., Urai, J.L., Fiduk, J.C. and Kukla, P.A. (2019). Deformation of intrasalt competent layers in different modes of salt tectonics. *Solid Earth*, 10(4), 987–1013. https://doi.org/10.5194/se-10-987-2019

Smith, D.B. and Crosby, A. (1979). The regional and stratigraphical context of Zechstein 3 and 4 potash deposits in the British sector of the southern North Sea and adjoining land areas. *Economic Geology*, 74(2), 397–408.

Stewart, S.A. and Coward, M.P. (1995). Synthesis of salt tectonics in the southern North Sea, UK. *Marine and Petroleum Geology*, 12(5), 457–475.

Strozyk, F., van Gent, H., Urai, J.L. and Kukla, P.A. (2012). 3D seismic study of complex intra-salt deformation: an example from the Upper Permian Zechstein 3 stringer, western Netherlands. *Geological Society, London, Special Publications*, 363, 489–501.

Taylor, J.C.M. (1998). Upper Permian – Zechstein. In: Glennie, K.W. (ed.) *Petroleum Geology of the North Sea: Basic Concepts and Recent Advances*, 4th edn. Oxford: Blackwell Science, 174–211.

van Gent, H., Urai, J.L. and de Keijzer, M. (2011). The internal geometry of salt structures – a first look using 3D seismic data from the Zechstein of the Netherlands. *Journal of Structural Geology*, 33(3), 292–311.

Warren, J.K. (2006). *Evaporites: Sediments, Resources and Hydrocarbons*. Berlin: Springer.

Ziegler, P.A. (1990). *Geological Atlas of Western and Central Europe*, 2nd edn. The Hague: Shell Internationale Petroleum Maatschappij.

Supplemental Material for "Autogenic initiation of basin-scale salt tectonics"

Jimmy Moneron[1,2], Giridas Maiti[1], Mads Huuse[3], Christopher Aiden-Lee Jackson[4,5], Alexandre Lethiers[2], and Nevena Andrić-Tomašević[1]

[1]*Institute of Applied Geosciences, Karlsruhe Institute of Technology, Germany*
[2]*ISTeP, Sorbonne Université, CNRS, 75005, Paris, France*
[3]*Department of Earth and Environment, The University of Manchester, Manchester, UK*
[4]*WSP UK Ltd, 8 First Street, Manchester, M15 4RP, UK*
[5]*Landscape and Basins Research Group (LBRG), Department of Earth Science and Engineering, Imperial College London, London SW7 2AZ, UK*

1. SUPPLEMENTAL BACKGROUND

1.1. Zechstein stratigraphy and intrasalt heterogeneity

In the North Sea the Zechstein Supergroup (ZSG) comprises five stratigraphic units (Z1–Z5; Smith and Crosby, 1979; Geluk, 1999), each recording a cycle of carbonate, sulfate, halite, and K-Mg salt precipitation. The Z3 (*Leine*) cycle includes the ~50-m-thick, anhydrite-dominated Z3a (*Hauptanhydrit*), the 100–200-m-thick, halite-dominated Z3h, and the K-Mg-rich Z3k, which is locally up to 90 m thick (Smith and Crosby, 1979; Taylor, 1998). The Z3k is conformably overlain by the *Roter Salzton*, a ~15-m-thick, isopachous claystone marking the transition to the Z4 cycle (Richter-Bernburg, 1955).

The Z3a is regionally ~45–50 m thick, although it locally contains anomalously thick zones (ATZs) that are up to ~150 m thick (Fulda, 1929; van Gent et al., 2011; Moneron, 2025) and which form an interconnected network of sinuous ridges and elliptical mounds traceable for >100 km. Individual segments of the ATZ network extend for several tens of kilometers. ATZs are interpreted as syn-depositional gypsum buildups (Moneron, 2025).

Primary gypsum (c. 2.3 g/cm³) is only marginally (7%) denser than halite (c. 2.15 g/cm³), but its conversion to anhydrite (c. 2.95 g/cm³) imposes a contrast of c. 700 kg/m³, 37% greater than halite, while synchronously reducing solid volume by 30%–40% (Borchert and Muir, 1964; Jackson and Hudec, 2017). In the context of the ZSG, Moneron and Jackson (2025) used seismic-stratigraphic techniques to date the conversion of the Z3a gypsum to anhydrite to the time of Z3h deposition, after c. 300 m of burial. Aldridge et al. (2026) then showed that the resulting densification folded the stringer itself, generating 1–2 km wavelength intrasalt synclines cored by ATZs, with negligible lateral shortening, no orientation bias, and demonstrably predating regional salt tectonics.

1.2. Mechanisms of regional folding

Salt mobilization in the Southern Permian Basin (SPB) began in the Triassic across most sub-basins, and proceeded in pulses through Jurassic rifting, Late Cretaceous to Paleocene inversion, and locally into the Cenozoic (Harding and Huuse, 2015; Brennan and Adam, 2023; Gaitan and Adam, 2023).

Four mechanisms have usually been invoked, all allogenic: gravity gliding on the tilted Zechstein detachment (Stewart and Coward, 1995), differential loading by the overburden (Gaitan and Adam, 2023), reactivation of sub-salt faults during Sub-Hercynian and Laramide shortening (Deckers and van der Voet, 2018), and whole-lithosphere buckling under far-field stresses (Cloetingh et al., 1999). Each predicts folds whose pattern is set by an external control: the dip of the detachment, the depocenter geometry, the basement fault grid, or the regional stress field. The one intrasalt mechanism proposed so far, diagenetic densification of the stringer (Aldridge et al., 2026), operates solely within the salt; and although syn-depositional relief is known to localize overlying Triassic minibasins (Joffe et al., 2023), the salt has never been considered a source of the deformation it records.

2. SUPPLEMENTAL DATA

2.1. Seismic data

This study uses 26,533 km² of three-dimensional (3-D) seismic reflection data from the UK and Dutch sectors of the Southern North Sea (Fig. S1). The UK dataset (~16,000 km²) is drawn principally from the PGS Southern North Sea MegaSurvey, a merge of 86 individual pre-stack time-migrated surveys rebinned to a common datum and phase. The Dutch dataset (~10,000 km²) comprises five surveys released through the TNO/NLOG public repository. All volumes are zero-phase and are displayed

with SEG normal polarity, so that downward increases and decreases in acoustic impedance correspond to positive and negative reflections, respectively. Bin spacing is 25 × 25 m throughout.

Resolution within the dataset varies because each component survey was processed with its own parameters, including dominant frequency. At the intra-Zechstein level, a dominant frequency of 25–30 Hz is combined with interval velocities of ~5000–6000 m/s. The corresponding limit of separability (λ/4), below which the top and base reflections of the Z3a interfere and its thickness cannot be measured independently, is ~42–60 m. The limit of visibility (λ/8), the thinnest interval still producing a detectable amplitude response, is ~21–30 m. Lateral resolution is set by the 25 m bin spacing.

Because the component surveys retain their individual acquisition and processing parameters, amplitude scaling and frequency content vary between sub-areas. Analyses that depend on absolute amplitude, principally the root-mean-square (RMS) extractions used to delineate the ATZ network where the Top Z3a is discontinuous, were therefore performed survey by survey and compared qualitatively; they are not merged into a single quantitative amplitude grid. Thickness-based analyses, which depend on reflection timing rather than amplitude, are unaffected and carry the quantitative argument.

2.2. Well data

Thirty-four boreholes calibrate the interpretation: 24 in the UK sector, released through the North Sea Transition Authority (NSTA), and 10 in the Dutch sector, released through TNO/NLOG (Fig. S1). Wells were selected on penetration of a seismically resolved Z3a interval and on the availability of a composite log suite. Reported formation tops follow the operator composite logs, cross-checked against the national stratigraphic nomenclatures.

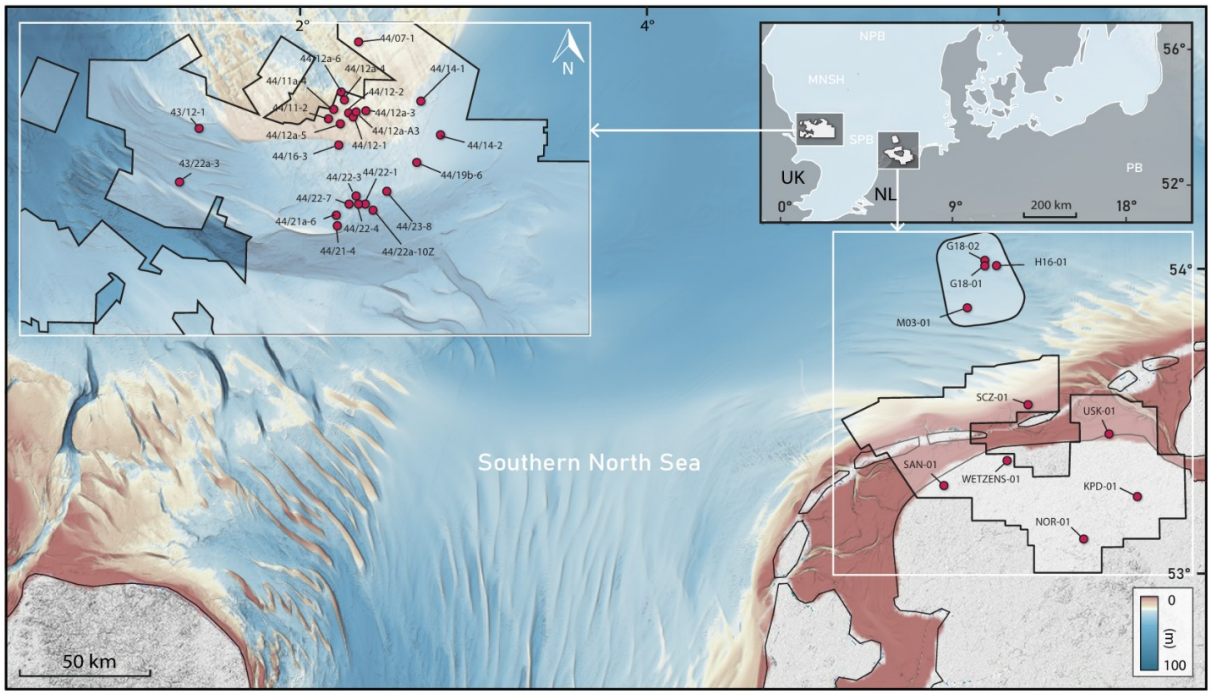


Fig. S1. Seismic and well database. Outlines of the 3-D surveys interpreted in the UK (left) and Dutch (right) sectors of the Southern North Sea, with the 34 calibration wells (circles). Inset: regional setting (MNSH, Mid North Sea High; NPB, Northern Permian Basin; SPB, Southern Permian Basin; PB, Polish Basin). Bathymetry in meters.

3. SUPPLEMENTAL METHODS

3.1. Chrono- and seismo-stratigraphic framework

Interpretation is referred to the chrono- and lithostratigraphic schemes of the UK and Dutch sectors, which differ in nomenclature but are correlative at the level of the horizons mapped here (Fig. S2A). The two schemes are placed on a common absolute time scale so that equivalent units can be read directly against one another: the Zechstein Group (NL) and Zechstein Group (UK) are a single body, the Lower and Upper Germanic Trias groups correspond to the Bacton and Haisborough groups, and the Rijnland Group corresponds to the Cromer Knoll Group. Within the Zechstein, the Z1–Z5 cycles and the position of the Z3a (Hauptanhydrit) between the Grauer Salzton and the Z3 halite are shown in Figure S2B, together with the reflections picked at its top and base.

3.2. Seismic-to-well tie

All boreholes were used to calibrate the seismic data, selected on the availability of sonic, density and gamma-ray logs and on penetration of a seismically resolved Z3a interval. Synthetic seismograms were generated from the sonic and density logs, referenced to seismic datum using check-shot and vertical seismic profile (VSP) data where available, and convolved with a bandpass wavelet matched to the frequency content of the data at the target level.

The ties confirm the polarity and log expression of each mapped surface (Figs. S2A, S3). The Top Z3a corresponds to a positive-amplitude reflection marking the downward transition from Z3 halite into anhydrite, expressed as a sharp downward increase in density and decrease in sonic transit time. The Base Z3a corresponds to a negative-amplitude reflection at the anhydrite–Z2 halite contact, accompanied by a downward increase in gamma ray across the basal Grauer Salzton and Plattendolomit (cf. Moneron, 2025). The Base Zechstein and Top Zechstein were tied to the Top Rotliegend and the Base Triassic respectively, and the Top Bunter (= Base Rijnland) and Base Cretaceous (= Base Chalk) were calibrated as laterally continuous markers within the post-salt succession.

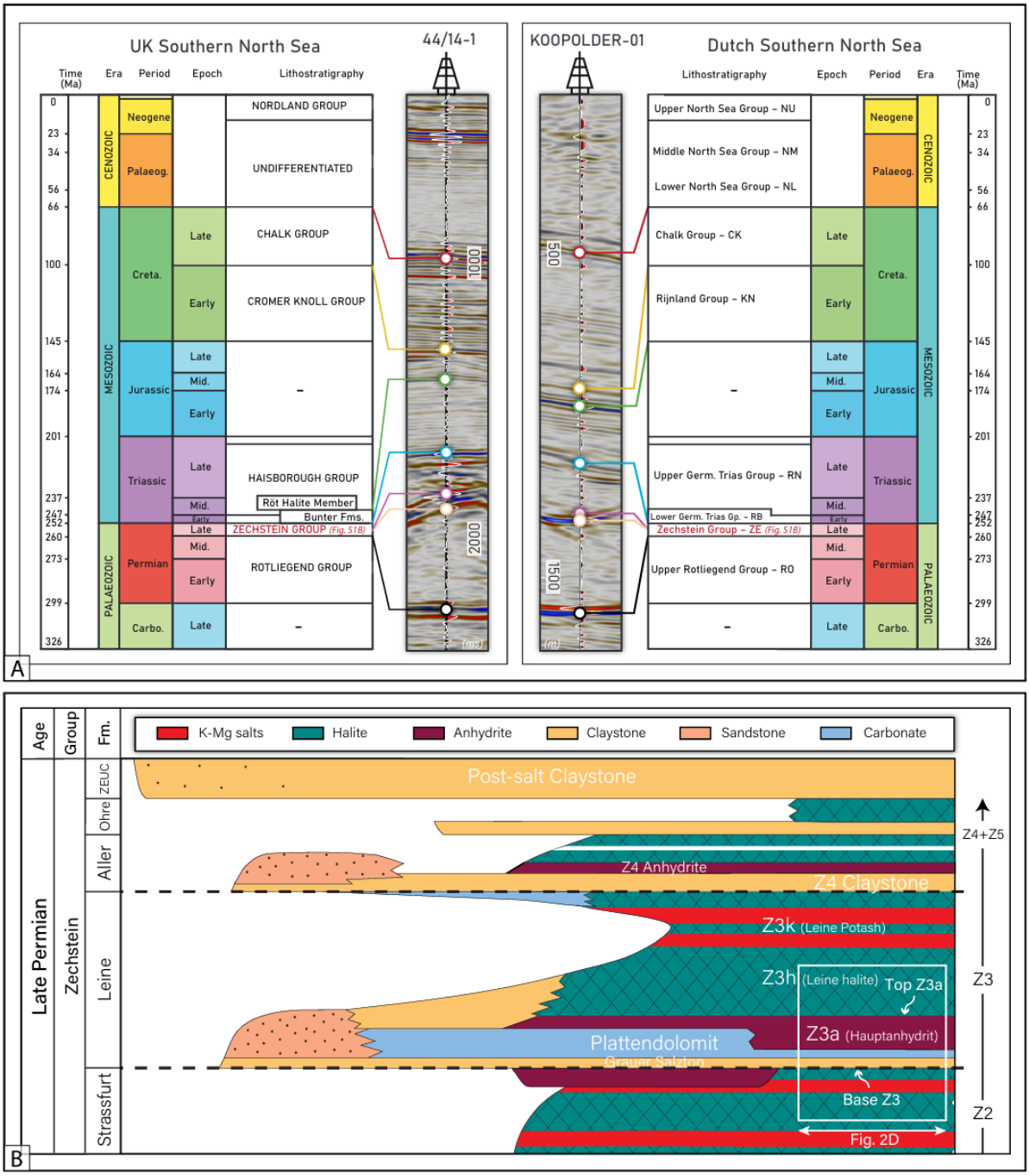


Fig. S2. Stratigraphic framework. (A) Chrono- and lithostratigraphy of the UK (left) and Dutch (right) Southern North Sea on a common time scale, tied to wells 44/14-1 (TWT) and Koopolder-01 (depth); colored markers are the horizons mapped in this study. (B) Zechstein lithostratigraphy, showing the Z3a (Hauptanhydrit) and the interval imaged in Figure 2D.

3.3. Horizon interpretation

Six horizons were calibrated against wells and mapped regionally: Base Zechstein, Base Z3a, Top Z3a, Top Zechstein (= Base Triassic), Top Bunter (= Base Rijnland), and Base Cretaceous (= Base Chalk). Interpretation began on a manual grid of ~200 × 200 m and was densified by seeded autotracking, with a correlation threshold of ~0.8 to limit interpolation. The Top Z3a was picked on a 50 m grid prior to autotracking because its amplitude is sensitive to tuning as the unit thickens.

Where the Z3a is strongly deformed or its bounding reflections are discontinuous, principally within salt-cored anticlines and along welds, mapping confidence is low and these areas were excluded from the quantitative analysis. In such areas, and along the steeply dipping flanks of the thickest ATZs

where the Top Z3a becomes disjointed from its base, RMS amplitude extraction on the more continuous Base Z3a surface was used to support interpretation: thickened anhydrite along ATZs produces a distinct impedance contrast with the capping halite and delineates the network independently of the thickness map (Moneron, 2025).

3.4. ATZ identification

ATZ polygons were extracted from the Z3a isopach by thresholding. The mapped grid comprises 42,452,480 bins of 25 × 25 m (625 m² each), covering 26,533 km². A threshold of 55 m was selected from the bin thickness distribution (Fig. 2E) and from previous ATZ studies (van Gent et al., 2011; Strozyk et al., 2014; Moneron, 2025).

This choice is constrained by resolution as well as by the distribution. Because the limit of separability at this level is ~50 m, a Z3a at its regional background thickness lies at or just below tuning, and its apparent thickness in seismic data is therefore not independently resolved. This accounts for the offset between the background thickness derived from seismic data (45–50 m; Fig. 2E) and the slightly greater value obtained from wells (Moneron, 2025). Setting the threshold at 55 m ensures that every interval classified as an ATZ exceeds the limit of separability, so that its mapped thickness reflects genuine geometry rather than tuning.

The threshold is conservative in one direction only: intervals between ~50 and 55 m that are genuinely thickened are classified as background, so the mapped network is a minimum estimate of the true ATZ population. No interval classified as an ATZ can be an artifact of tuning.

3.5. Thickness mapping

Three isopachs underpin the analysis:

- Gross Zechstein (Base to Top Zechstein), characterizing the wavelength, amplitude and position of the salt-cored anticlines, walls and welds that define the present structural configuration.
- Z3a (Base Z3a to Top Z3a), including the Grauer Salzton and Plattendolomit, from which ATZs are delineated using the 55 m threshold. This value is the upper limit of the background thickness population, whose mode lies at 45–50 m (Fig. 2E), and not the background thickness itself.
- Post-salt overburden (Top Zechstein to Top Bunter, and Top Bunter to Base Cretaceous), used to test for depositional thickening above the sites of inferred depressions and for its upward decay.

3.6. Testing for syn-depositional subsidence

The central observation of this study, that ATZs foundered and generated accommodation at the top-salt surface, requires that depressions be demonstrated independently of later halokinesis, which also thickens overburden into synclines. Three criteria were applied.

First, analysis was restricted to sub-areas of modest Top Zechstein deformation, where later salt flow was limited and early geometries are most likely to be preserved (cf. Aldridge et al., 2026).

Second, thickening was assessed stratigraphically. An early, ATZ-driven depression predicts that excess thickness is concentrated in the lowermost overburden package and decays upward, whereas later halokinetic subsidence predicts thickening distributed through younger intervals and coeval with the growth of the long-wavelength folds.

Third, internal reflection geometries within the basal overburden were examined for onlap onto the flanks of the mapped lows, and for truncation over the intervening highs. Together these record infill of pre-existing relief rather than passive draping or later structural sagging.

3.7. Numerical modeling

Approach

The numerical models test whether the density contrast imposed by the conversion of gypsum to anhydrite is sufficient to make ATZs founder into the surrounding halite, and how lateral connectivity between ATZs controls that foundering and the relief it produces. The simulations begin after conversion: the ATZs are already anhydrite and are embedded in halite (Fig. 4A, Stage 1). Two configurations are compared. In the reference model (Type-1, attached) the ATZs are attached to a continuous anhydrite layer representing the background Z3a. In Type-2 (detached) models, identical ATZs are detached from that layer.

Governing equations

Because inertial forces are negligible at geological strain rates, the models solve the incompressible Stokes equations for conservation of momentum and mass:

$$-\nabla p + \nabla\cdot(2\eta\dot{\varepsilon}) + \rho\mathbf{g} = 0 \tag{S1}$$

$$\nabla\cdot\mathbf{v} = 0 \tag{S2}$$

where p is pressure, η the effective dynamic viscosity, ρ density, $\mathbf{g}$ gravitational acceleration, $\mathbf{v} = (u, v)$ the velocity vector with horizontal and vertical components u and v, and $\dot{\varepsilon} = \frac{1}{2}[\nabla\mathbf{v} + (\nabla\mathbf{v})^{\mathrm{T}}]$ the strain-rate tensor. For a two-dimensional Newtonian medium, the deviatoric stresses are $\tau_{xx} = 2\eta\,\partial u/\partial x$, $\tau_{yy} = 2\eta\,\partial v/\partial y$ and $\tau_{xy} = \eta(\partial u/\partial y + \partial v/\partial x)$, and the momentum equations become:

$$-\partial\tau_{xx}/\partial x - \partial\tau_{xy}/\partial y + \partial p/\partial x = 0 \tag{S3}$$

$$-\partial\tau_{xy}/\partial x - \partial\tau_{yy}/\partial y + \partial p/\partial y = \rho' g \tag{S4}$$

where ρ' is the density relative to the reference halite density. The vertical coordinate increases downward, so positive vertical velocity corresponds to sinking. Because buoyancy is expressed relative to halite, the pressure p solved in Eq. S4 is the dynamic pressure: the departure of total pressure from the lithostatic state of a halite column.

Numerical implementation

The equations are discretized by finite differences on a staggered marker-and-cell grid (Gerya and Yuen, 2003). Material properties are carried by Lagrangian markers advected with the computed velocity field (Gerya and Yuen, 2007). The domain is 5 km wide and 1 km deep, resolved at 10 m (500 × 100 cells), with 3 × 3 Lagrangian markers per grid cell. The timestep is dynamically restricted using a Courant–Friedrichs–Lewy (CFL) criterion with a CFL coefficient of 0.20 and is additionally limited to a maximum of 100 yr. This ensures that marker displacement during an individual timestep remains small relative to the numerical grid spacing. The discretized system is solved using the direct sparse solver spsolve from the SciPy library, with the pressure null space constrained using a Lagrange multiplier.

Geometry and initial conditions

Four ATZs, each 200 m wide and 150 m thick, are centered at x = 1, 2, 3 and 4 km, between 350 and 500 m depth. In the reference model they are linked by a continuous, 50-m-thick anhydrite layer along their base (450–500 m depth) that extends across the domain. In Type-2 models this layer is absent, and the ATZs are isolated bodies of identical size, density and viscosity. All other parameters are identical between the two configurations.

Material properties

Both phases are linear (Newtonian) viscous fluids (Table S2). Halite has a density of 2200 kg m^{-3} and a viscosity of 10^{17} Pa s, within the range estimated for rock salt (van Keken et al., 1993; Urai et al., 2008).

Anhydrite has a density of 2900 kg m^{-3} and a viscosity of 10^{19} Pa s; this hundredfold contrast is consistent with the competence of intrasalt sulfate layers (Rowan et al., 2019). The resulting density contrast is 700 kg m^{-3}, with g = 9.81 m s^{-2}. A linear rheology is appropriate for the onset of foundering, when differential stresses are highest; its limitations for long-term behavior are discussed in Section 5.2.

Boundary conditions

Free-slip boundary conditions are imposed on all four boundaries (left, right, top, and bottom), allowing tangential motion while preventing normal flow. In Type-1 models where the anhydrite blocks are connected by a basal anhydrite layer, the lateral free-slip boundaries influence the sinking behavior of the outermost ATZ blocks. These blocks behave as effectively disconnected bodies from one side and sink faster, approaching the base of the salt layer, whereas the central blocks, mechanically connected through the basal anhydrite layer, remain suspended ~200 m above it. Consequently, quantitative comparisons of sinking rates and deformation are restricted to the two central ATZ blocks to minimize boundary effects.

Model phases

In Phase 1 (density-driven foundering), the model evolves from its initial configuration for 200 k.y. (Fig. 4A, Stages 1–3). In Phase 2 (sediment loading), the deformed configuration at the end of Phase 1 is used as the initial condition. The material above the deformed marker horizon, initially located 200 m below the model top, is replaced with sand (density = 2400 kg/m^3; viscosity = 10^{19} Pa·s), while the deformed evaporite geometry below this horizon is preserved. To suppress further density-driven foundering during Phase 2, density contrasts between the evaporite units are removed while retaining their viscosity contrasts. This allows the subsequent deformation to be driven primarily by sediment loading rather than continued gravitational sinking of the anhydrite blocks. The sand layer has a spatially variable thickness reflecting the deformation developed during Phase 1. The model then evolves for a further 1 m.y. (Fig. 4A, Stages 4–5; Fig. S12).

Sensitivity experiments

Starting from the reference model, one parameter was varied at a time: the density contrast, the viscosity contrast, the width and thickness of the ATZs, and their spacing (ranges in Table S3).

Diagnostics

Three quantities are extracted and compared between configurations at matched elapsed times (0, 65, 135 and 200 k.y.):

(1) **Sinking velocity:** the vertical velocity field (positive downward; Fig. S11), and the depth of the base of each ATZ through time, measured on the model frames (Fig. S9).

(2) **Dynamic pressure:** p from Eq. S4, in MPa, after removal of the domain mean, since pressure in incompressible flow is defined only to within a constant. Both configurations are displayed on a common color scale. Peak values at ATZ corners, and where an ATZ rests on the base of the model, are numerical stress concentrations and are excluded from comparisons. Anomalies are characterized in the surrounding halite by their peak value and width at half maximum (Fig. S10).

(3) **Relief:** the depth and width of the depressions or minibasins formed above the sinking ATZ bodies, measured along a passive marker horizon initially positioned at a depth of 350 m and subsequently advected with the modeled material flow.

Table S2. Material properties of the reference model.

Property	Halite	Anhydrite
Density, ρ (kg m^{-3})	2200	2900
Dynamic viscosity, η (Pa s)	10^{17}	10^{19}
Constitutive behavior	Newtonian viscous	Newtonian viscous
Viscosity relative to halite	1	100

Density contrast $\Delta\rho$ = 700 kg m^{-3}; g = 9.81 m s^{-2}.

Table S3. Parameter ranges of the sensitivity experiments.

Parameter	Reference value	Range tested
Density contrast, $\Delta\rho$ (kg m^{-3})	700	200–700
Viscosity contrast, anhydrite/halite	100	100–10,000
ATZ width (m)	200	100–500
ATZ thickness (m)	150	50–150
ATZ spacing (km)	1	0.5–2
Viscosity of connecting layer (Pa s)	10^{19}	10^{19}–10^{21}
Connectivity	Attached	Attached / detached

4. SUPPLEMENTAL RESULTS

4.1. Uninterpreted and enlarged seismic sections

Figures S3 and S4 reproduce, at larger scale and with minimal annotation, the sections presented in Figures 2D and 3 of the main text. They are provided so that the reflection terminations on which the interpretation rests (onlap onto the flanks of ATZ-cored lows, and truncation beneath the Base Cretaceous over the intervening highs) can be assessed independently of the interpretation drawn on them.

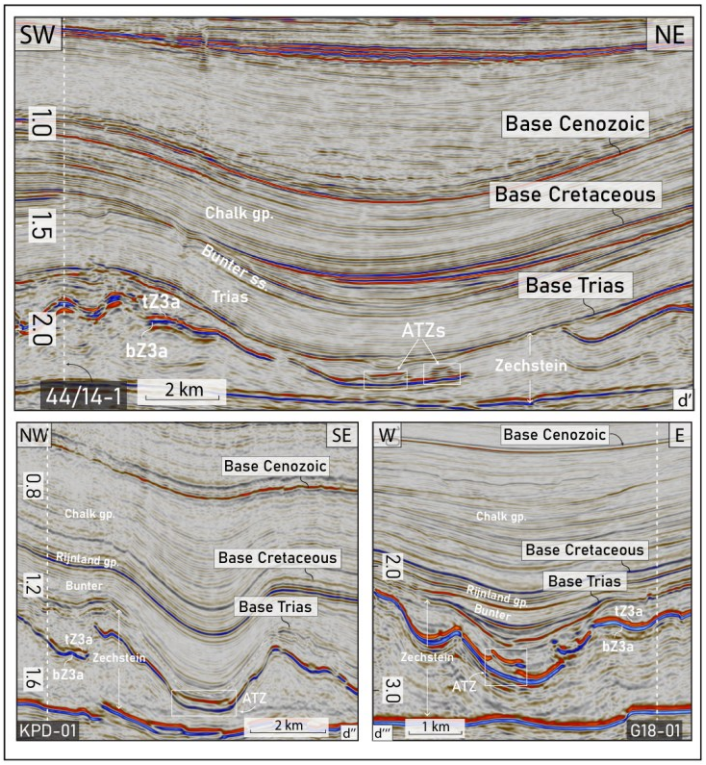


Fig. S3. Regional sections d′, d″ and d‴ of Figure 2D, enlarged. ATZs (boxes) occupy the cores of synclines whose axes persist upward to the Base Cenozoic. Wells 44/14-1, KPD-01 and G18-01. tZ3a, bZ3a: top and base Z3a.

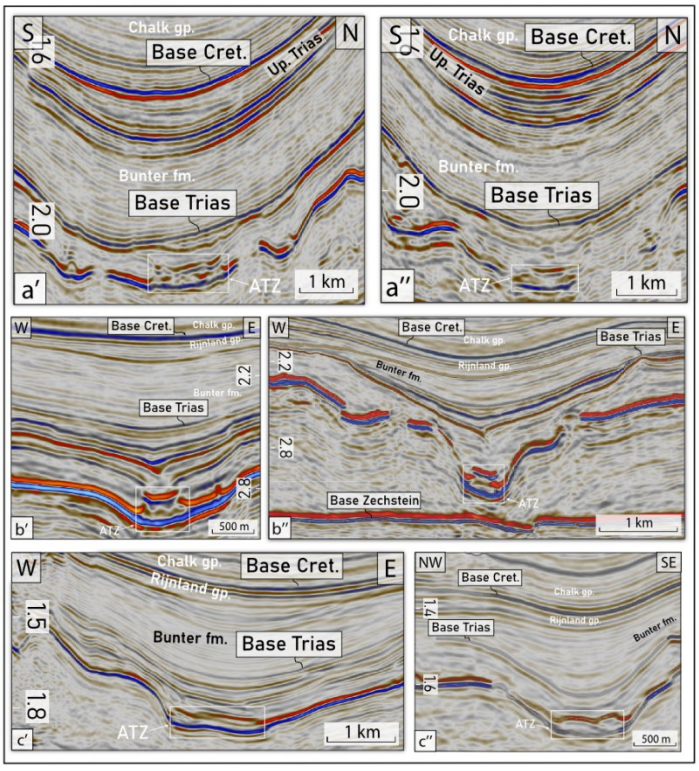


Fig. S4. Sections a′–c″ of Figure 3, enlarged. Lower Triassic strata onlap the flanks of ATZ-cored lows (a′, a″, b′) and are truncated beneath the Base Cretaceous over the intervening highs (b″, c′, c″).

4.2. Enlarged maps with transparent ATZ networks

In Figure 3 the ATZ network is drawn over structure and thickness maps of stratigraphically shallower horizons, a presentation that aids comparison but that could be read as imposing the correspondence it

is intended to show. Figure S5 therefore pairs each map with an enlarged view in which the ATZ network is transparent. The syncline axes, and the branching and segmentation of the lows, are equally apparent in these views.

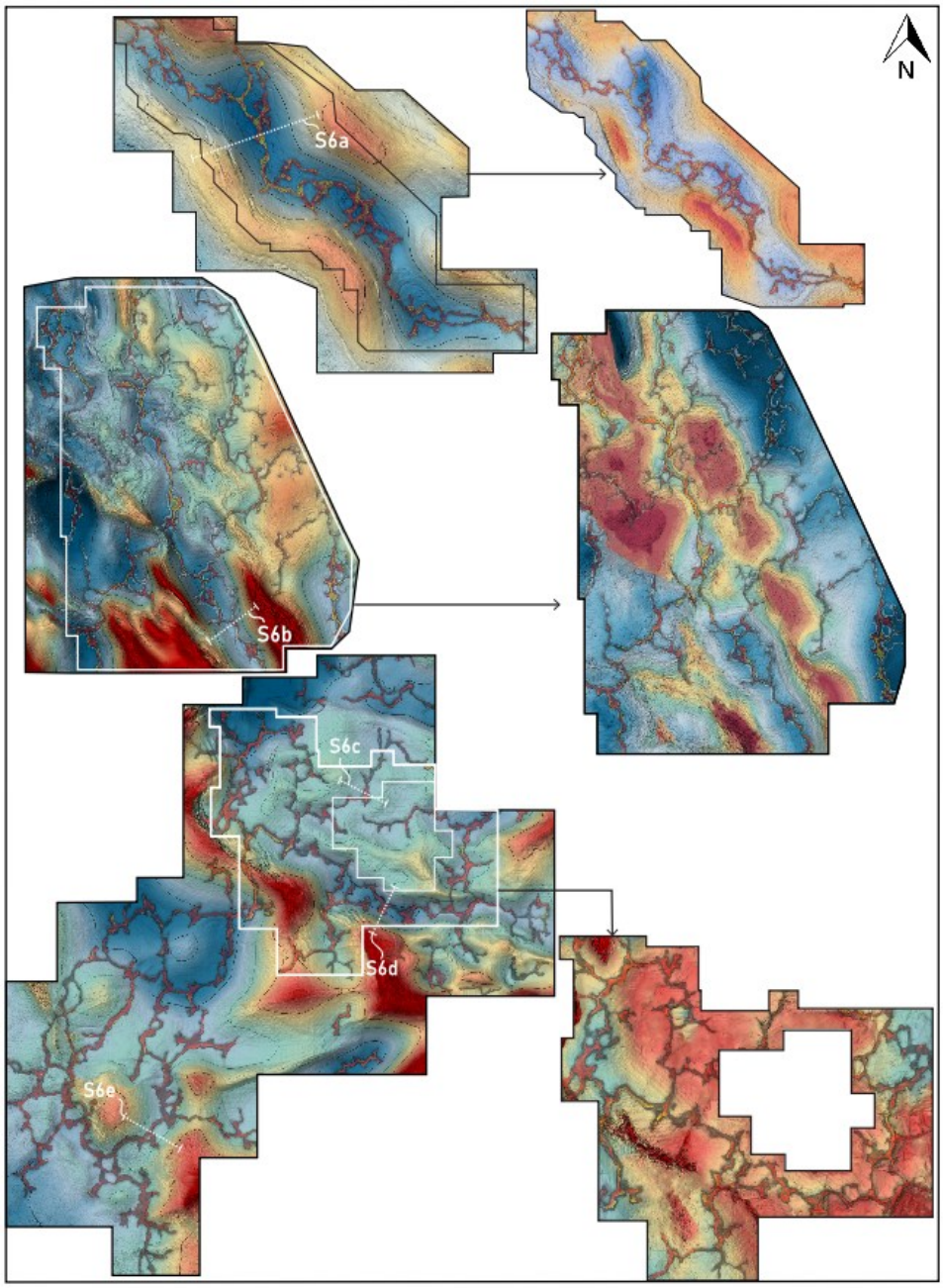


Fig. S5. Structure and thickness maps of Figure 3 with the ATZ network superimposed. Dashed lines locate the sections of Figure S6.

4.3. Regional expression of the synclines

Five sections, located on Figure S5, show in section the structures the maps express in plan view (Fig. S6). In each the Base Zechstein is near-planar while the Top Zechstein is folded into a syncline, so that the Zechstein thins beneath the axis and thickens into the flanking highs; in the most strongly developed example the residual salt beneath the axis approaches a weld (Fig. S6e). Where the Z3a remains resolved it is segmented and lies at or near the base of the thinned interval (Figs. S6a, S6b).

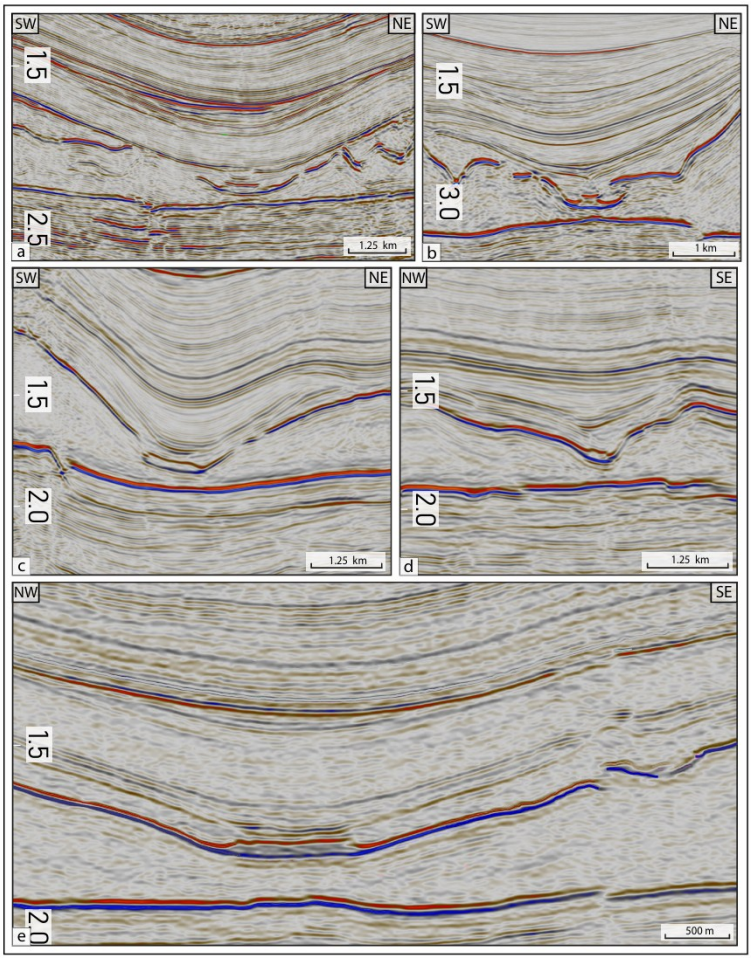


Fig. S6. Regional sections across the mapped synclines, located on Figure S5. The Base Zechstein (lowermost pick) is near-planar in all five, while the Top Zechstein and the overlying markers are folded into synclines beneath which the Zechstein thins, locally toward a weld (e). Vertical scale in seconds TWT except for b which is in km.

4.4. Synclines lacking an underlying ATZ

Synclines of comparable wavelength and amplitude occur across both sectors with no ATZ in their hinge, and these provide the internal control for the analysis (Fig. S7). Where an ATZ is absent, the Triassic maintains its regional isopachous thickness across the structure, its internal reflections remain parallel and conformable through the hinge, and no onlap is developed against the flanks. Truncation beneath the Base Cretaceous is present over the crests of these structures, as it is elsewhere, but is not accompanied by the complementary onlap in the adjacent low. The two geometries that together record differential movement during deposition are therefore not developed. Such synclines deform a succession that was already in place, rather than preserving one that accumulated as they subsided.

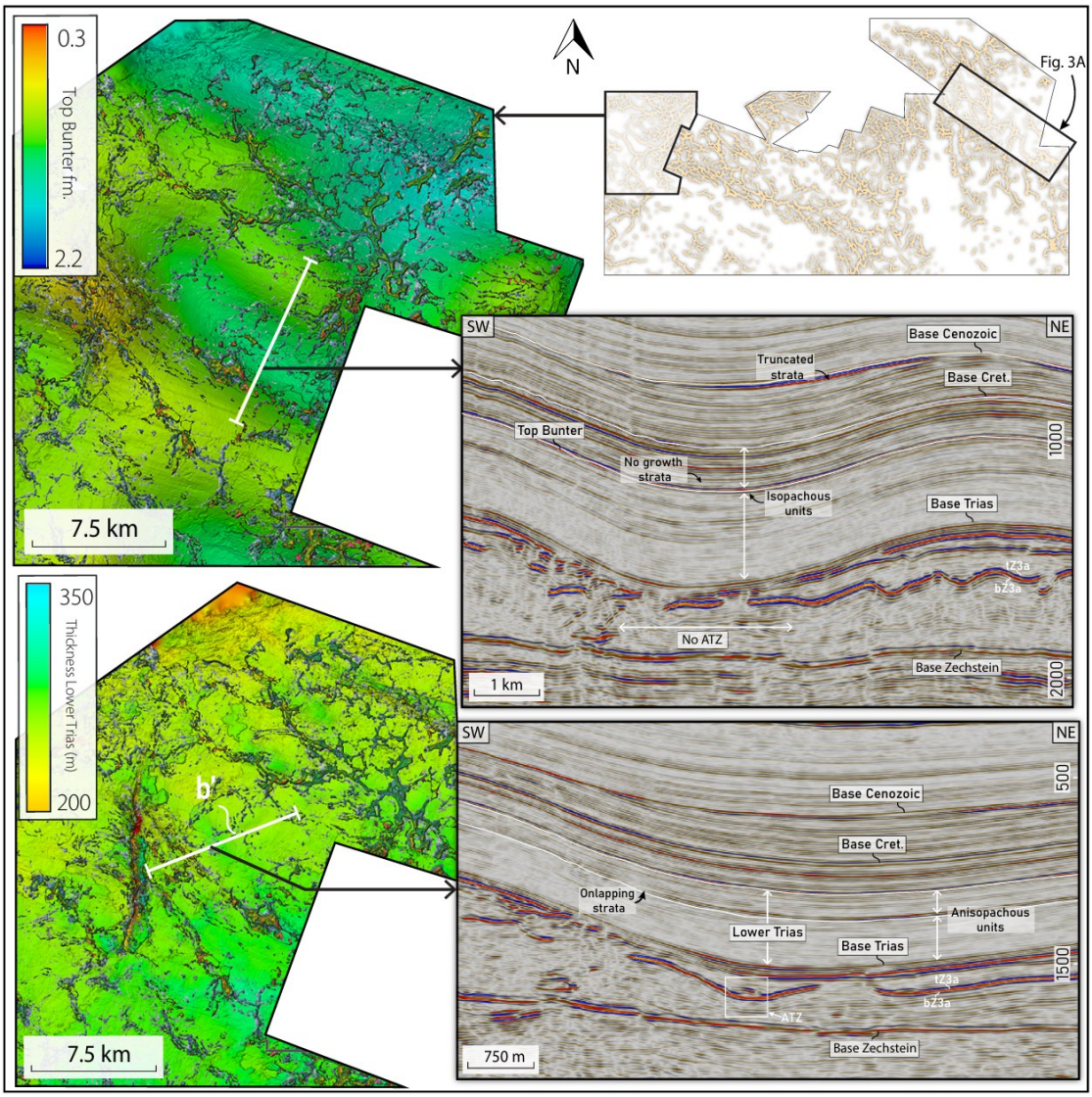


Fig. S7. Synclines with and without an underlying ATZ. Top: a syncline with no ATZ in its hinge; Triassic units are isopachous through the structure and no growth strata are developed. Bottom: an ATZ-cored syncline in the same area, with lower Triassic strata thickening into the low and onlapping its flanks. Maps are Top Bunter time-structure and Lower Triassic thickness.

4.5. Isolated ATZs at the base of the salt

A small number of ATZs occur as isolated bodies, laterally detached from the Z3a, which is absent or unresolved on either side (Fig. S8). These differ from their connected counterparts in one respect, and it is the diagnostic one: they rest at or immediately above the Base Zechstein reflection, having descended through the full thickness of the underlying halite, whereas ATZs retained within a continuous sheet are found suspended several hundred meters above it (Figs. 2D, S3). The same contrast is produced by the control experiment (Fig. S9), in which identical bodies reach the base of the model within 135 k.y. when detached, but remain ~200 m above it after 200 k.y. when attached. The natural population therefore reproduces, at basin scale, the dependence of foundering on sheet connectivity that the models isolate.

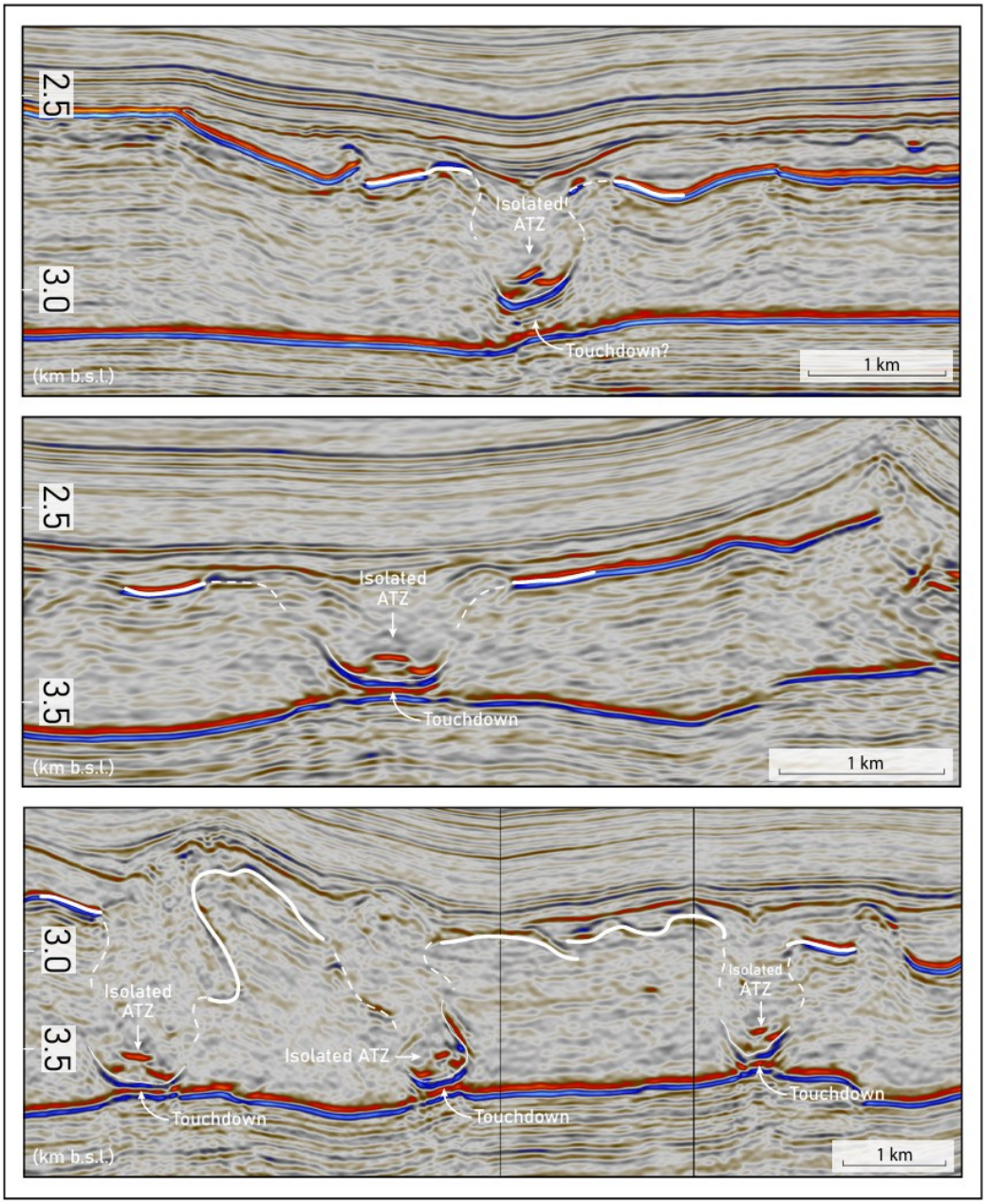


Fig. S8. Isolated ATZs that have reached the base of the salt. In each section the thickened body is detached from the adjacent Z3a (dashed) and rests on the Base Zechstein reflection ("touchdown"), in contrast to the suspended position of ATZs within a continuous sheet. Depth in km below sea level.

4.6. Control experiments

Effects of basal anhydrite layer connectivity

At equal elapsed times the detached bodies descend faster and further than their attached counterparts (Fig. S9). The bases of the central detached bodies sink from 500 m to ~805 m depth within 65 k.y. (~4.7 mm/yr on average), and by 135 k.y. all four detached bodies lie within ~25 m of the base of the model. The bases of the two central attached bodies reach ~620, ~705 and ~805 m depth at 65, 135 and 200 k.y. (~1.2–1.9 mm/yr), and at the end of Phase 1 lie ~200 m above the base of the model, still sinking.

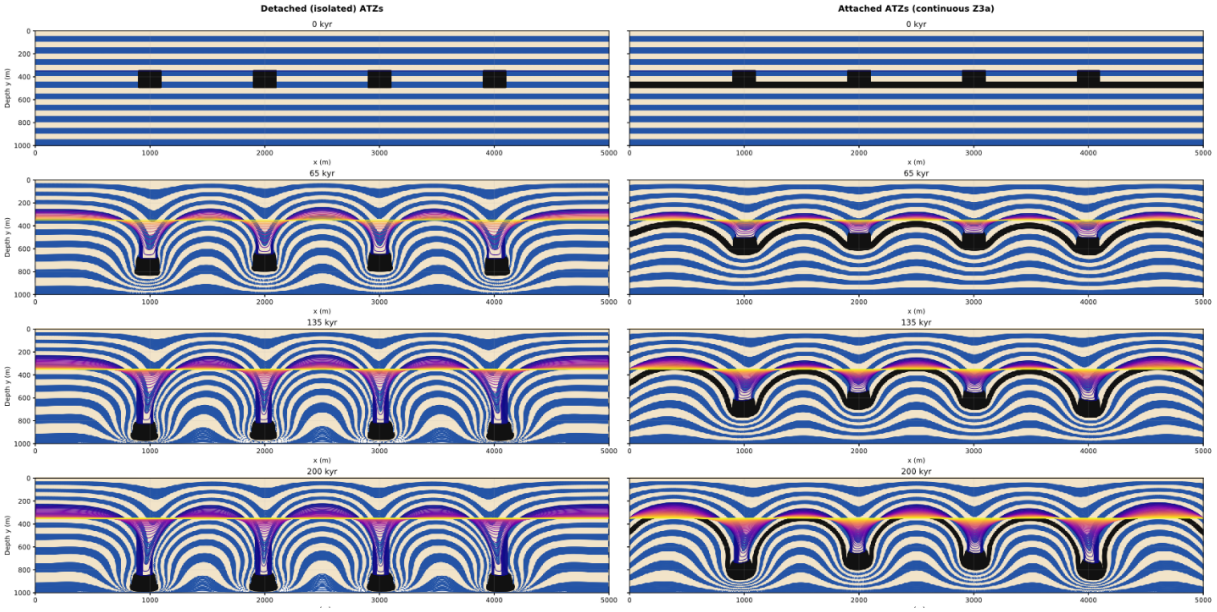


Fig. S9. Effect of stringer connectivity. Material evolution of the detached (left) and attached (right) experiments at 0, 65, 135 and 200 k.y.; anhydrite in black, halite with passive marker layers.

Dynamic pressure fields

The dynamic pressure field, defined as the deviation of total pressure from the lithostatic reference state, differs between the two configurations in the way the anomaly is distributed rather than in its magnitude (Fig. S10). About a detached body the anomaly is sharply confined, a negative lobe surmounting a positive one over a radius comparable to the body itself. Where the segments remain connected, an anomaly of comparable magnitude is distributed along the length of the sheet, which deflects over a wavelength several times the width of the individual bodies. At 65 k.y., 60 m beneath the central ATZs, the positive anomaly reaches ~0.3 MPa with a width at half maximum of ~0.4 km about a detached body, against ~0.2 MPa and ~2.8 km where the bodies are attached; above the bodies it is ~−0.2 MPa in both.

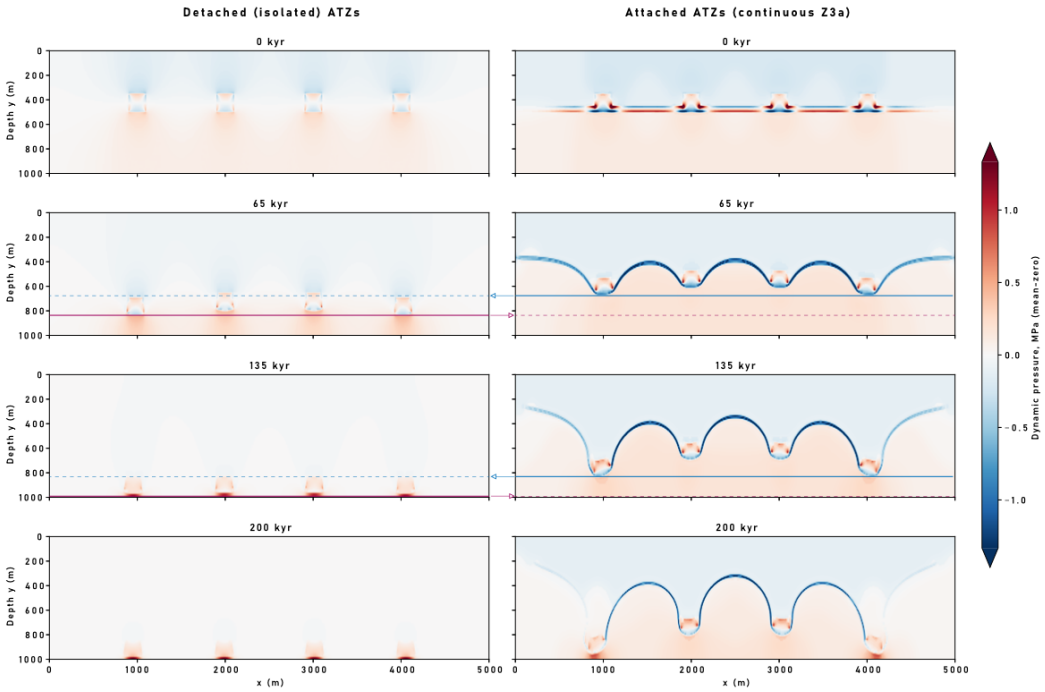


Fig. S10. Dynamic pressure (mean-zero) in the detached (left) and attached (right) experiments at 0, 65, 135 and 200 k.y., on a common color scale; values beyond ±1.3 MPa, at ATZ corners and basal contacts, are saturated. At 65 and 135 k.y., solid lines mark the depth of the deepest ATZ in each configuration, and dashed lines repeat it in the other panel for comparison.

Sinking velocity fields

The vertical velocity fields record the same contrast (Fig. S11). At the start of the experiment detached ATZs sink at up to ~5.4 mm/yr and attached ATZs at up to ~3.5 mm/yr. Detached ATZs have almost stopped by 135 k.y., once they rest on the base of the model, whereas the central attached ATZs are still sinking at up to ~2.5 mm/yr after 200 k.y. In both configurations halite rises between and beside the sinking bodies.

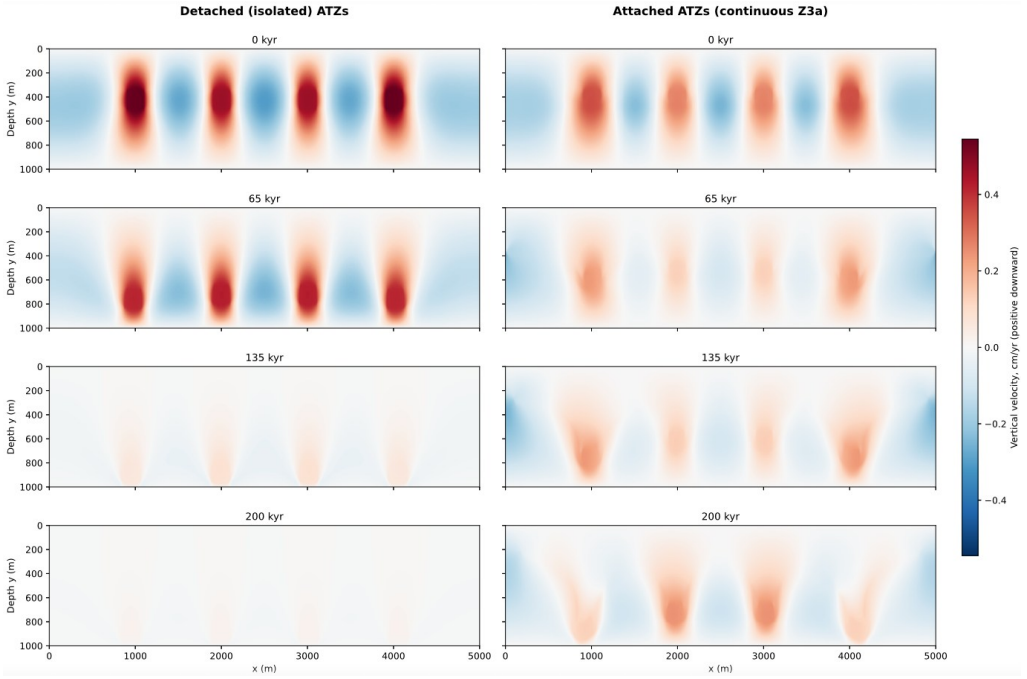


Fig. S11. Vertical velocity in the detached (left) and attached (right) ATZ experiments at 0, 65, 135 and 200 k.y., shown on a common color scale (positive downward). Detached ATZs sink faster, initially ~0.54 cm/yr against ~0.35 cm/yr when

attached. They have almost stopped by 135 k.y., once they reach the base of the salt. Attached ATZs sink more slowly but are still descending at 200 k.y. Blue areas mark halite rising between and beside the sinking bodies.

4.7. Complete model evolution

Figure 4A presents five stages of the reference experiment. Figure S12 gives its complete material evolution, at 0, 65, 135 and 200 k.y. in Phase 1 and at 0, 335, 665 and 1000 k.y. in Phase 2.

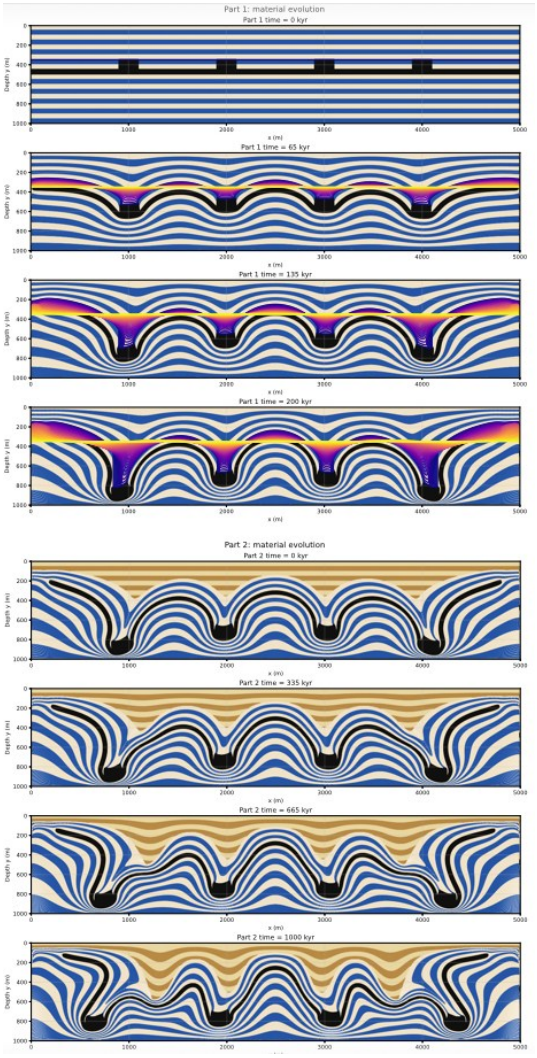
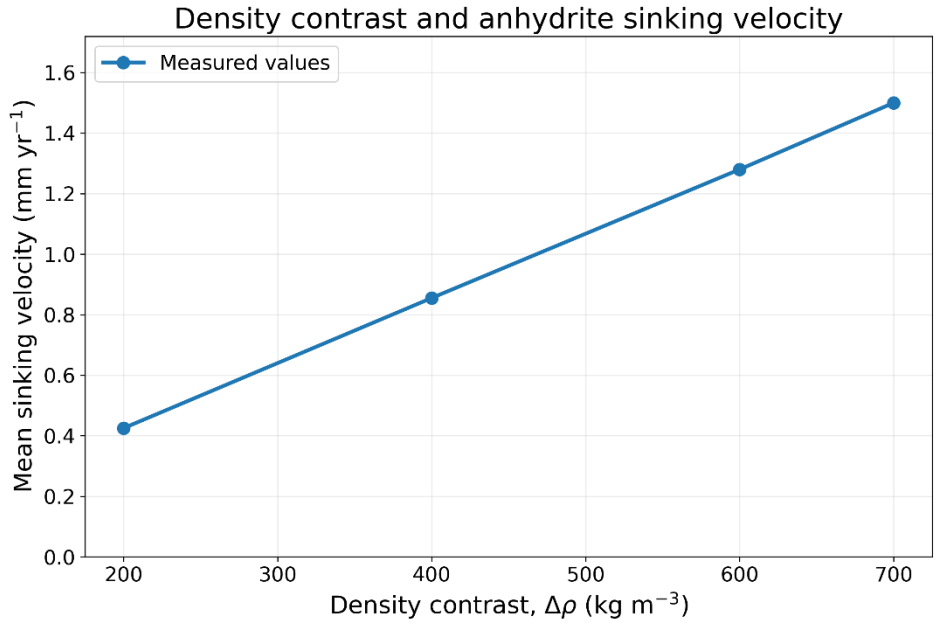


Fig. S12. Material evolution of the reference (attached) experiment during Phase 1 (Fig. 4A, Stages 1–3; density-driven foundering; 0–200 k.y.) and Phase 2 (Stages 4–5; sand loading; 0–1000 k.y. after the end of Phase 1).

4.8. Sensitivity test results

***Density and viscosity contrasts*.** Increasing the density contrast between anhydrite and the surrounding halite accelerates gravitational sinking, whereas reducing the density contrast decreases the sinking velocity (Fig. S13). This behavior reflects the greater negative buoyancy of denser anhydrite bodies. In the reference configuration, the density contrast is 700 kg/m³, with additional experiments examining contrasts of 200 to 600 kg/m³. Increasing the viscosity of the anhydrite blocks relative to the surrounding halite reduces their sinking velocity (Fig. S13). The viscosity-ratio experiments show that this reduction is most pronounced at relatively low viscosity ratios, whereas further increases in block viscosity produce progressively smaller changes in sinking velocity. Together, these experiments indicate that density contrast controls the gravitational driving force, while viscosity contrast regulates the resistance to deformation and the rate of foundering.



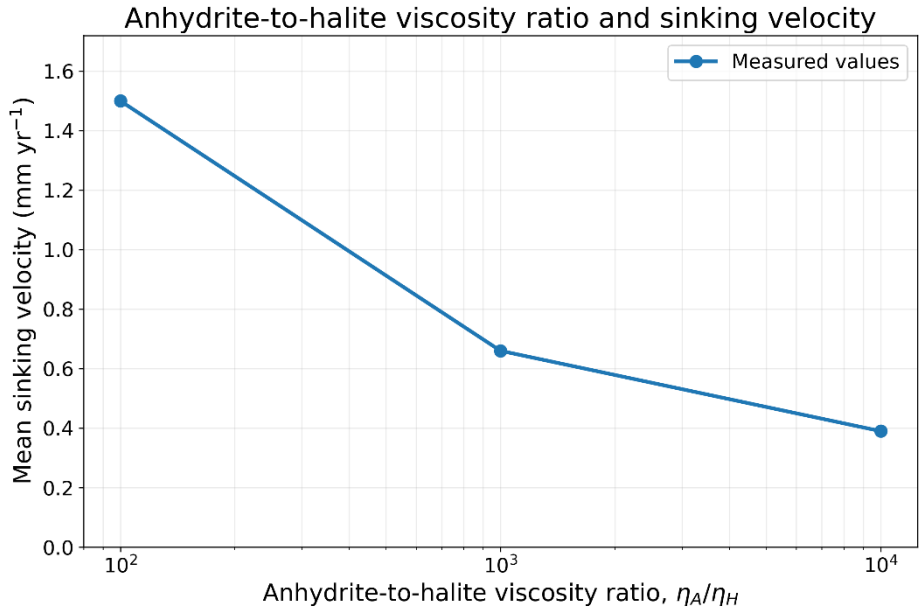


Fig. S13. Effects of density contrast (keeping viscosity ratio constant at 100) and viscosity ratio (keeping density contrasts constant at 700 kg/m3) on anhydrite sinking velocity in the reference models. The measured values represent the mean sinking velocity of the two central anhydrite blocks.

Anhydrite connectivity. The mechanical connection between anhydrite blocks through a basal anhydrite layer strongly influences their sinking behavior. In models containing disconnected blocks, individual anhydrite bodies sink more freely through the surrounding halite (Figs. S9–S11). In contrast, connected blocks deform collectively, with the inter-connecting basal layer resisting differential vertical displacement. Consequently, the central connected blocks remain suspended ~200 m above the salt base, whereas effectively disconnected outer blocks can descend almost to the base. Increasing the viscosity of the connecting layer further inhibits sinking by increasing its resistance to deformation. These experiments demonstrate that the continuity and mechanical strength of the basal

anhydrite layer can significantly restrict gravitational foundering, even when the density contrast between anhydrite and halite remains unchanged.

Anhydrite-block size. Variations in the dimensions of the anhydrite blocks influence both their sinking behavior and the geometry of the overlying synclinal depressions (Fig. S14). Larger blocks produce broader and generally more pronounced depressions, whereas smaller blocks generate narrower, more localized deformation (Fig. S15). These differences reflect variations in the magnitude and spatial distribution of the gravitational forcing associated with the sinking bodies. Block size therefore influences the amplitude and lateral extent of the developing synclines and the resulting accommodation space available for sediment accumulation.

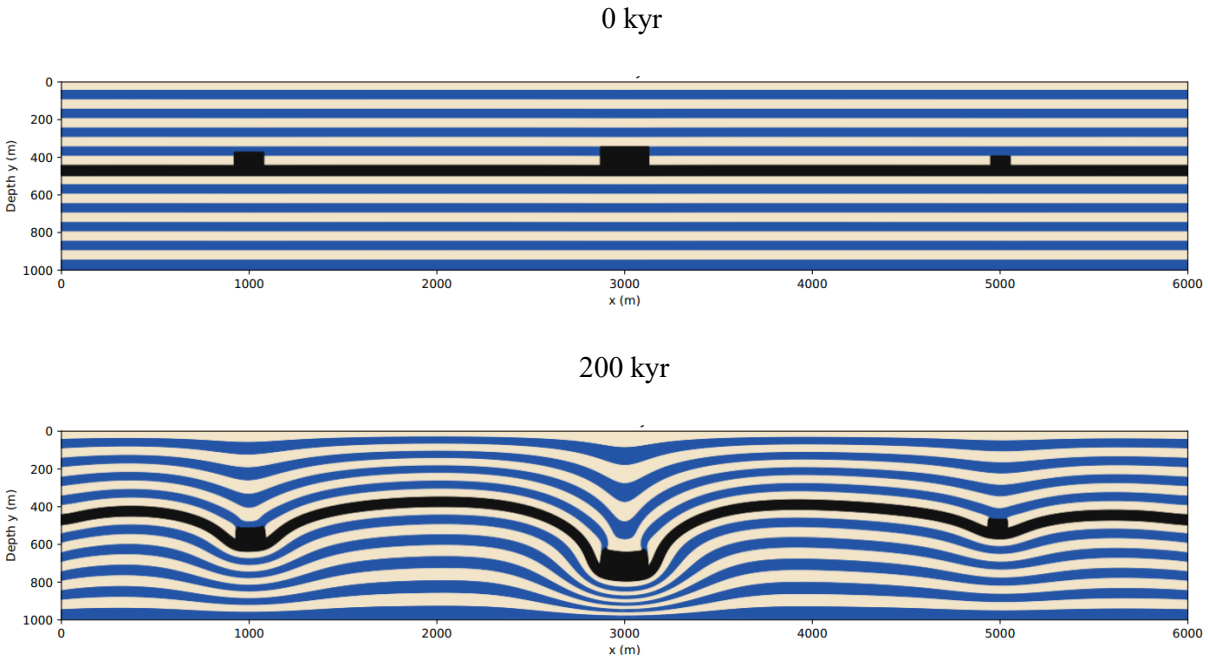


Fig. S14. Effect of anhydrite block geometry on sinking behavior and overlying synclinal depressions. The model contains three anhydrite blocks of different dimensions: left (l = 150 m, h = 120 m), middle (l = 250 m, h = 150 m), and right (l = 100 m, h = 100 m), where l and h denote block length and height, respectively. The blocks exhibit different sinking rates, illustrating the influence of block geometry on gravitational sinking through halite.

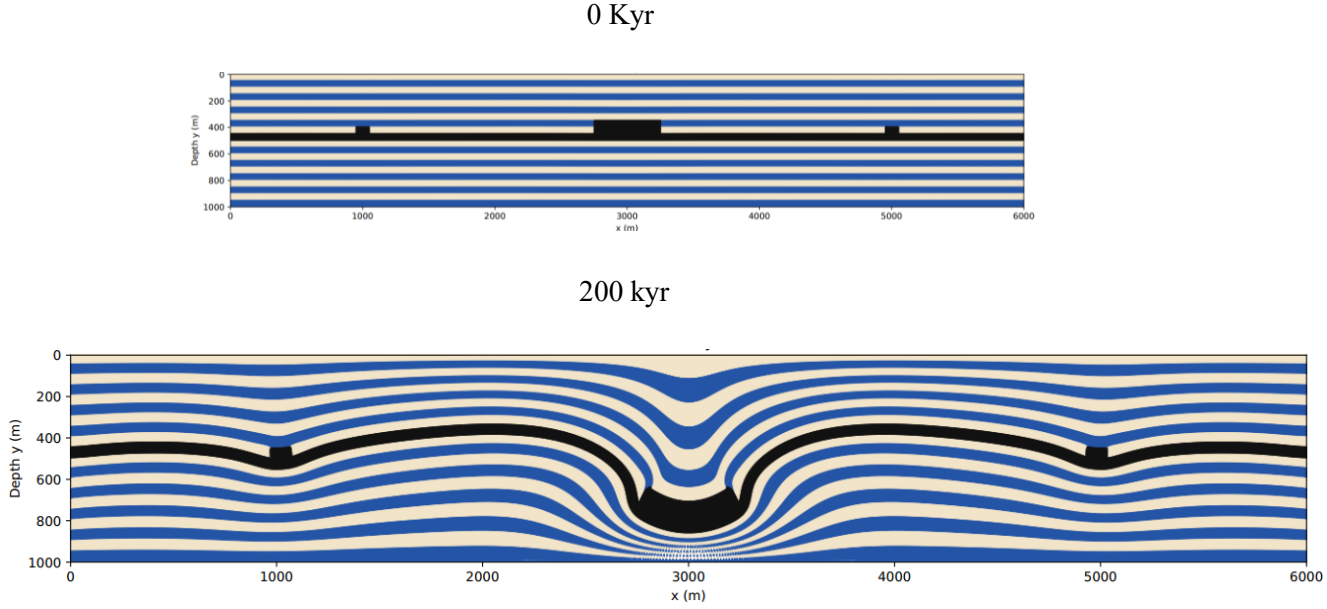


Fig. S15. Effect of anhydrite block size on overburden basin geometry. The model contains three anhydrite blocks of different dimensions: left and right (l = 100 m, h = 100 m) and middle (l = 500 m, h = 150 m), where l and h denote block length and height, respectively. The larger central block sinks faster and produces a broader and deeper overburden depression than the two smaller flanking blocks, demonstrating the influence of block size on sinking velocity and the geometry of the resulting surface deformation.

Block spacing. The spacing between adjacent anhydrite blocks primarily controls the wavelength of the overlying syncline–anticline system (Fig. S16). Closely spaced blocks generate shorter-wavelength deformation, with adjacent depressions and intervening highs occurring over relatively small lateral distances. Increasing the separation between blocks produces a corresponding increase in the spacing of the overlying folds. In the reference models, characteristic depression widths are approximately 400–500 m, although these vary with the imposed block geometry and spacing. These experiments indicate that the spatial distribution of ATZs plays an important role in determining the lateral organization of minibasin systems.

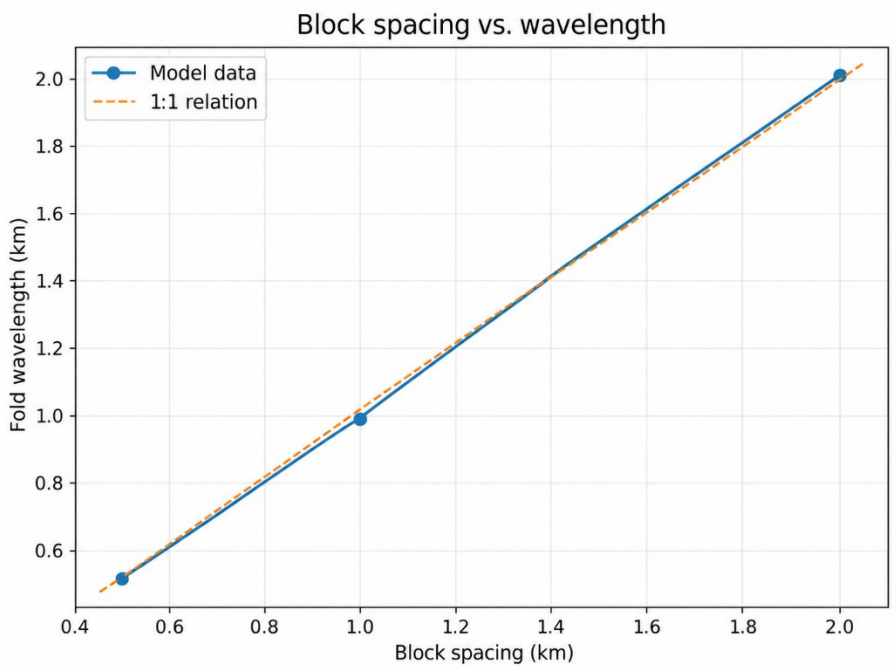


Fig. S16. Effect of anhydrite block spacing on the wavelength of overburden folds. The model results closely follow the 1:1 relationship (dashed line), indicating that fold wavelength is primarily controlled by the spacing between adjacent anhydrite blocks.

Overall, the sensitivity experiments reveal that different parameters govern distinct aspects of the evolving deformation. Density and viscosity contrasts primarily determine the rate of anhydrite sinking, while the continuity and strength of the basal anhydrite layer regulate the extent to which individual blocks can founder independently. In contrast, block dimensions and spacing predominantly influence the amplitude and wavelength of the resulting synclinal depressions. These relationships suggest that the geometry of minibasin systems reflects not only the gravitational instability of dense anhydrite bodies within halite, but also their initial distribution and mechanical connectivity.

5. SUPPLEMENTAL IMPLICATIONS, LIMITATIONS AND OPEN QUESTIONS

5.1. Implications

Intrasalt heterogeneity has generally been read as a passive record of salt flow (Strozyk et al., 2012; Raith et al., 2016). Our results reverse that relationship for the earliest increment of deformation: the internal stratigraphy of a layered evaporite sequence, and the diagenetic history of its sulfate layers, can determine where the first structures develop in the overburden above it. In the SPB, this gives the mapped ATZ network predictive value. Because ATZ-cored synclines mark where salt was first withdrawn, and where welds and salt-thickness minima are therefore most likely, the network offers a basis for anticipating these features ahead of drilling, with bearing on seal continuity for CO_2 and hydrogen storage and on the siting of solution caverns (Caglayan et al., 2020).

The mechanism is not specific to the Zechstein. Any basin in which sulfate was deposited as gypsum of laterally variable thickness, and later converted to anhydrite within halite, carries the same latent instability (Warren, 2006; Célini et al., 2024). In such basins the timing of that conversion, rather than the onset of regional tectonism, may set the clock for the first increment of salt movement, and the geometry of the sulfate, rather than that of the basement or the overburden, may set its pattern.

5.2. Limitations

The numerical models are deliberately simple, and four simplifications should be noted. None alters the first-order result, that densified ATZs founder and deflect the depositional surface above them, but each bears on the details.

First, the models are two-dimensional. A polygonal network in three dimensions will distribute stress and compete for salt differently from a layer deflecting in section (Fernandez et al., 2020), and is likely to modify the amplitude and width of the depressions; it cannot, however, remove the density contrast that drives them.

Second, halite is treated as a Newtonian fluid. This is appropriate for the onset of foundering, when differential stresses are highest and halite flow can be represented by a single effective viscosity, but not for the long-term arrest of attached ATZs, which reflects the stress dependence of halite creep at low differential stress (Li and Urai, 2016; Rowan et al., 2019). Experiments with a composite flow law, combining pressure-solution and dislocation creep, would test this directly.

Third, the models include neither insoluble residue nor compaction, so soft welding (Wagner and Jackson, 2011) and the evolving strength of the clastic fill are not represented. Both act late in the evolution, after the depressions have formed.

Fourth, the domain is only 5 km wide, and its free-slip side walls act as mirror planes, so the outermost ATZs are less restrained than the central ones and sink faster (Section 3.7). Quantitative comparisons therefore rely on the central ATZs.

5.3. Open questions

The threshold separating ATZs that organize overburden structure from those that do not is identified here only in outline. Its dependence on ridge width, continuity and burial rate, and on the thickness of halite beneath the ATZs, remains to be established, and three-dimensional experiments with stress-

dependent rheology are the natural next step. Testing whether ATZ-cored synclines are absent where the underlying salt is thin, or where the sulfate was never gypsum, would provide an independent check on the mechanism in other evaporite basins.

SUPPLEMENTAL REFERENCES CITED

Aldridge, B., Stewart, S., Phillips, D., Foschi, M. and Cartwright, J. (2026). A new mode of syn-depositional folding in the Zechstein Supergroup due to differential loading and diagenetically induced density inversion. *Journal of Structural Geology*, 203, 105606. https://doi.org/10.1016/j.jsg.2025.105606

Borchert, H. and Muir, R.O. (1964). *Salt Deposits: The Origin, Metamorphism and Deformation of Evaporites*. London: Van Nostrand.

Brennan, C. and Adam, J. (2023). Regional variability of onset and cessation of salt tectonics in the Mesozoic and Cenozoic Southern North Sea subbasins. *AAPG Bulletin*, 107(12), 2169–2196.

Caglayan, D.G., Weber, N., Heinrichs, H.U., Linßen, J., Robinius, M., Kukla, P.A. and Stolten, D. (2020). Technical potential of salt caverns for hydrogen storage in Europe. *International Journal of Hydrogen Energy*, 45, 6793–6805.

Célini, N., Pichat, A. and Ringenbach, J.-C. (2024). Salt tectonics synchronous with salt deposition in the Santos Basin (Ariri Formation, Brazil). *Earth and Planetary Science Letters*, 641, 118853. https://doi.org/10.1016/j.epsl.2024.118853

Cloetingh, S., Burov, E. and Poliakov, A. (1999). Lithosphere folding: primary response to compression? (from central Asia to Paris basin). *Tectonics*, 18(6), 1064–1083. https://doi.org/10.1029/1999TC900040

Deckers, J. and van der Voet, E. (2018). A review on the structural styles of deformation during Late Cretaceous and Paleocene tectonic phases in the southern North Sea area. *Journal of Geodynamics*, 115, 1–9.

Fernandez, N., Hudec, M.R., Jackson, C.A.-L., Dooley, T.P. and Duffy, O.B. (2020). The competition for salt and kinematic interactions between minibasins during density-driven subsidence: observations from numerical models. *Petroleum Geoscience*, 26(1), 3–15. https://doi.org/10.1144/petgeo2019-051

Fulda, E. (1929). Über Anhydrit-Klippen. *Kali*, 23, 129–133.

Gaitan, G. and Adam, J. (2023). Extent and variability of Mesozoic–Cenozoic multi-stage salt diapirs in the Southern Permian Basin, Southern North Sea. *Basin Research*, 35(6), 2078–2117. https://doi.org/10.1111/bre.12791

Geluk, M.C. (1999). Late Permian (Zechstein) rifting in the Netherlands: models and implications for petroleum geology. *Petroleum Geoscience*, 5(2), 189–199.

Gerya, T.V. and Yuen, D.A. (2003). Characteristics-based marker-in-cell method with conservative finite-differences schemes for modeling geological flows with strongly variable transport properties. *Physics of the Earth and Planetary Interiors*, 140, 293–318. https://doi.org/10.1016/j.pepi.2003.09.006

Gerya, T.V. and Yuen, D.A. (2007). Robust characteristics method for modelling multiphase visco-elasto-plastic thermo-mechanical problems. *Physics of the Earth and Planetary Interiors*, 163, 83–105. https://doi.org/10.1016/j.pepi.2007.04.015

Harding, R. and Huuse, M. (2015). Salt on the move: multi stage evolution of salt diapirs in the Netherlands North Sea. *Marine and Petroleum Geology*, 61, 39–55.

Jackson, M.P.A. and Hudec, M.R. (2017). *Salt Tectonics: Principles and Practice*. Cambridge: Cambridge University Press.

Joffe, A., Jackson, C.A.-L. and Pichel, L.M. (2023). Syn-depositional halokinesis in the Zechstein Supergroup (Lopingian) controls Triassic minibasin genesis and location. *Basin Research*, 35(2), 784–801.

Li, S. and Urai, J.L. (2016). Numerical modelling of gravitational sinking of anhydrite stringers in salt (at rest). *Bollettino di Geofisica Teorica ed Applicata*, 57(3), 233–246.

Moneron, J. (2025). Major heterogeneity in evaporitic depositional systems: the genesis of kilometre-scale gypsum networks in the Zechstein Basin. *Global and Planetary Change*, 246, 104710. https://doi.org/10.1016/j.gloplacha.2025.104710

Moneron, J. and Jackson, C.A.-L. (2025). Basin-scale development of giant collapse structures induced by gypsum diagenesis. *Geology*, 53(8), 673–678. https://doi.org/10.1130/G53338.1

Raith, A.F., Strozyk, F., Visser, J. and Urai, J.L. (2016). Evolution of rheologically heterogeneous salt structures: a case study from the NE Netherlands. *Solid Earth*, 7(1), 67–82. https://doi.org/10.5194/se-7-67-2016

Richter-Bernburg, G. (1955). Stratigraphische Gliederung des deutschen Zechsteins. *Zeitschrift der Deutschen Geologischen Gesellschaft*, 105, 843–854.

Rowan, M.G., Urai, J.L., Fiduk, J.C. and Kukla, P.A. (2019). Deformation of intrasalt competent layers in different modes of salt tectonics. *Solid Earth*, 10(4), 987–1013. https://doi.org/10.5194/se-10-987-2019

Smith, D.B. and Crosby, A. (1979). The regional and stratigraphical context of Zechstein 3 and 4 potash deposits in the British sector of the southern North Sea and adjoining land areas. *Economic Geology*, 74(2), 397–408.

Stewart, S.A. and Coward, M.P. (1995). Synthesis of salt tectonics in the southern North Sea, UK. *Marine and Petroleum Geology*, 12(5), 457–475.

Strozyk, F., van Gent, H., Urai, J.L. and Kukla, P.A. (2012). 3D seismic study of complex intra-salt deformation: an example from the Upper Permian Zechstein 3 stringer, western Netherlands. *Geological Society, London, Special Publications*, 363, 489–501.

Strozyk, F., Urai, J.L., van Gent, H., de Keijzer, M. and Kukla, P.A. (2014). Regional variations in the structure of the Permian Zechstein 3 intrasalt stringer in the northern Netherlands: 3D seismic interpretation and implications for salt tectonic evolution. *Interpretation*, 2(4), SM101–SM117. https://doi.org/10.1190/INT-2014-0037.1

Taylor, J.C.M. (1998). Upper Permian – Zechstein. In: Glennie, K.W. (ed.) *Petroleum Geology of the North Sea: Basic Concepts and Recent Advances*, 4th edn. Oxford: Blackwell Science, 174–211.

Urai, J.L., Schléder, Z., Spiers, C.J. and Kukla, P.A. (2008). Flow and transport properties of salt rocks. In: Littke, R. et al. (eds) *Dynamics of Complex Intracontinental Basins: The Central European Basin System*. Berlin: Springer, 277–290.

van Gent, H., Urai, J.L. and de Keijzer, M. (2011). The internal geometry of salt structures – a first look using 3D seismic data from the Zechstein of the Netherlands. *Journal of Structural Geology*, 33(3), 292–311.

van Keken, P.E., Spiers, C.J., van den Berg, A.P. and Muyzert, E.J. (1993). The effective viscosity of rocksalt: implementation of steady-state creep laws in numerical models of salt diapirism. *Tectonophysics*, 225, 457–476.

Wagner, B.H. and Jackson, M.P.A. (2011). Viscous flow during salt welding. *Tectonophysics*, 510(3–4), 309–326. https://doi.org/10.1016/j.tecto.2011.07.012

Warren, J.K. (2006). *Evaporites: Sediments, Resources and Hydrocarbons*. Berlin: Springer.